university of groningen

University Medical Center Groningen

University of Groningen

Flow and bubble statistics of turbulent bubble-laden downflow channel

Cifani, P.; Kuerten, J. G.M.; Geurts, B. J.

Published in:
International Journal of Multiphase Flow

DOI:
10.1016/j.ijmultiphaseflow.2020.103244

IMPORTANT NOTE: You are advised to consult the publisher's version (publisher's PDF) if you wish to cite from it. Please check the document version below.

Document Version
Publisher's PDF, also known as Version of record

Publication date:
2020

Link to publication in University of Groningen/UMCG research database

Citation for published version (APA):
Cifani, P., Kuerten, J. G. M., & Geurts, B. J. (2020). Flow and bubble statistics of turbulent bubble-laden downflow channel. *International Journal of Multiphase Flow*, *126*, [103244]. https://doi.org/10.1016/j.ijmultiphaseflow.2020.103244

Copyright
Other than for strictly personal use, it is not permitted to download or to forward/distribute the text or part of it without the consent of the author(s) and/or copyright holder(s), unless the work is under an open content license (like Creative Commons).

The publication may also be distributed here under the terms of Article 25fa of the Dutch Copyright Act, indicated by the “Taverne” license. More information can be found on the University of Groningen website: https://www.rug.nl/library/open-access/self-archiving-pure/taverne-amendment.

Take-down policy
If you believe that this document breaches copyright please contact us providing details, and we will remove access to the work immediately and investigate your claim.

Downloaded from the University of Groningen/UMCG research database (Pure): http://www.rug.nl/research/portal. For technical reasons the number of authors shown on this cover page is limited to 10 maximum.

Download date: 05-06-2022

International Journal of Multiphase Flow 126 (2020) 103244

Contents lists available at ScienceDirect

International Journal of Multiphase Flow

journal homepage: www.elsevier.com/locate/ijmulflow

Flow and bubble statistics of turbulent bubble-laden downflow channel

P. Cifani [a,*], J.G.M. Kuerten [b], B.J. Geurts [c,d]

[a] Computational Mechanics and Numerical Mathematics, University of Groningen, Nijenborgh 9, Groningen 9747AG, the Netherlands
[b] Mechanical Engineering, Eindhoven University of Technology, P.O. Box 513, Eindhoven 5600MB, the Netherlands
[c] Multiscale Modeling and Simulation, Faculty EEMCS, University of Twente, P.O. Box 217, Enschede 7500AE, the Netherlands
[d] Multiscale Physics of Energy Systems, Faculty of Applied Physics, Center for Computational Energy Research, the Netherlands

ARTICLE INFO

Article history:
Received 22 October 2019
Revised 20 January 2020
Accepted 10 February 2020
Available online 12 February 2020

Keywords:
Bubbly flow
Turbulent channel flow
DNS
Bubble statistics
Kinetic energy spectra

ABSTRACT

Direct numerical simulations of fully developed turbulent channel downflow at bulk Re equal to 6300, loaded with monodisperse bubbles at gas volume fractions $\alpha = 0.5\%$, $\alpha = 2.5\%$ and $\alpha = 10\%$ have been carried out. Bubble deformability, surface tension, as well as discontinuity in the material properties across the bubble interfaces are explicitly accounted for. A full-scale channel of size $4\pi H \times 2H \times 4\pi H/3$ in terms of the channel half-width H containing a number of bubbles up to $\mathcal{O}(10^3)$ is considered. The statistical structure of the bubbles, the probability density function describing the bubble velocity and the liquid kinetic energy spectra have been determined. A close range preferential clustering of the bubbles was found with a maximum density independent of the gas volume fraction at a separation distance of about $2.2R$, with R the bubble radius. Preferential horizontal alignment and a general tendency to repulsion is shown for separation distances smaller than $3R$. At larger separation distances a close to random distribution is observed for $\alpha = 2.5\%$ and $\alpha = 10\%$, while tendency to vertical alignment is observed for $\alpha = 0.5\%$. The pdf of the bubble velocity fluctuations was found to be well approximated by a Gaussian distribution. The liquid kinetic energy spectra in the channel core do not show a marked -3 scaling, which was previously reported for homogeneous isotropic turbulence and pseudo-turbulence.

© 2020 Elsevier Ltd. All rights reserved.

1. Introduction

Turbulent bubble-laden channel flow is of great interest from a fundamental point of view since it constitutes a confined energy system in which the essential features of turbulence and its interaction with dispersed bubbles can be studied. The simple geometry of the channel featuring periodicity in the stream-wise and span-wise directions allows to represent average quantities as one-dimensional profiles along the wall normal direction, which leads to a clear analysis of the flow statistics as documented over three decades of single-phase flow studies (Kim et al., 1987; Moser et al., 1999; Vreman and Kuerten, 2014).

Investigations of turbulent channel flows loaded with bubbles are relatively scarce compared to the volume of literature present for single-phase turbulence. Experiments on bubbly flows are particularly challenging given the current limitations of non-intrusive imaging techniques (Lau et al., 2013), often applicable only to very dilute void fractions (Mercado et al., 2010). In this respect, direct numerical simulation (DNS), where all the relevant scales of motion can be resolved on the computational grid at an appropriate time-step, offers numerous advantages (Tryggvason et al., 2013). In addition to the 3D Eulerian velocity field, the position and shape of all the bubbles are available in full detail at any simulated time instance, so that information on the bubble motion can be accurately collected. The considerable amount of required computational resources, however, has limited numerical studies to rather small domains and to a relatively small number of deformable bubbles in the range between 10 and 100 (Lu and Tryggvason, 2006; 2013). This limitation may even lead to qualitative shortcomings in the simulated flows. For example, in Roghair et al. (2011) lack of large-scale flow circulations due to the limited domain size was attributed to be the cause of considerable discrepancies between experimental and numerical results. In this paper we improve upon this situation and present a first simulation of turbulent bubble-laden downflow in which we generate the motion of a significant number of deformable bubbles in a large computational domain. The computational methodology and its high-performance parallel implementation (Cifani et al., 2018) allow a full detail analysis of the flow and bubble statistics, which can serve as point of refer-

* Corresponding author.
E-mail address: p.cifani@rug.nl (P. Cifani).

https://doi.org/10.1016/j.ijmultiphaseflow.2020.103244
0301-9322/© 2020 Elsevier Ltd. All rights reserved.

ence for further modeling of the properties of multiphase flow and as benchmark for new developments in simulation approaches.

The dynamics in a full-scale turbulent channel flow at bulk Reynolds number 6300 at a low, an intermediate and a high gas volume fraction of 0.5%, 2.5% and 10%, respectively, is investigated. This choice of domain and *Re* constitutes a well established single-phase reference flow to compare with (Vreman and Kuerten, 2014). The motion of the bubbles can be fully resolved in terms of tracking the two-phase interface. We account for bubble deformability as well as discontinuities in the material properties and surface tension. The simulations are carried out using the recently developed massively parallel bubbly-flow solver (Cifani et al., 2018), tailored to efficiently handle up to 10^4 bubbles in wall bounded turbulence. This flow solver makes a detailed investigation of turbulent bubble-laden channel flow possible over a wide range of gas volume fractions and extended time intervals, so that also reliable flow statistics can be determined. We simulate the multiple interaction of a significantly larger number of bubbles than previously considered in literature up to 1280 bubbles for the densest case. Furthermore, the analysis will not be limited to average liquid flow statistics, but a thorough investigation, at an unprecedented level of detail, of bubble structuring and scaling of the kinetic energy will be carried out, documenting turbulence modification arising from the embedded gas phase in the liquid flow.

In this work the bubble-laden flow is mathematically described by the so called "one-fluid formulation" of the governing equations (Prosperetti and Tryggvason, 2007), where the volume fraction field is used as a marker function of the second phase. This defines the Volume of Fluid (VOF) method (Hirt and Nichols, 1981; Rider and Kothe, 1998; Scardovelli and Zaleski, 1999) that we employ. The latter constitutes a well-established and widely used technique able to deliver a sharp gas-liquid interface by construction while retaining the theoretical order of accuracy upon grid refinement (Scardovelli and Zaleski, 2003; Liovic et al., 2006; Cifani et al., 2016). For completeness, we mention numerical studies of rising bubbles conducted by employing the Diffuse Interface method (Aland and Voigt, 2012; Wang et al., 2015) and the Lattice-Boltzmann method (Gupta and Kumar, 2008; Cheng et al., 2010; Fakhari et al., 2016). While relevant in their own right, maintaining sharp interfaces is challenging in both these latter approaches.

A comprehensive review of DNS of bubbly flows is presented in Tryggvason et al. (2013). In the work by Lu and Tryggvason (2006) a relatively small channel at $Re_\tau = 127$, referred to as the minimum channel flow, was simulated for 18 to 72 bubbles. The focus of this and successive studies of the same authors is mainly on the influence of the bubbles on first and second order flow statistics. Fundamentally different bubble organisation arises, comparing downflow configurations with upflow configurations. Some key observations are as follows. Migration of bubbles toward the core of the channel was observed in downflow and attributed to the lift force, leaving a bubble-free wall boundary layer. Also, compared to single-phase flow at the same Reynolds number a strong increase of the velocity fluctuations in the core of the channel was reported, which has been attributed to the generation of bubble wakes. Conversely, in upflow systems nearly spherical bubbles are driven towards the walls (Lu and Tryggvason, 2008). Furthermore, in the latter study the effect of deformability is investigated and found to reduce the lateral lift for strongly deformed bubbles. More recently, an upflow configuration for nearly spherical bubbles at $Re_\tau = 250$ has been investigated (Lu and Tryggvason, 2013), confirming clustering of the bubbles in the wall layer region. Nonetheless, as pointed out by these authors, the use of a minimum channel, in combination with the small number of bubbles (maximum equal to 140) raises questions about validity of the findings beyond the simulated conditions. This is a strong motivation for our current study in which we vary important parameters over a much wider range of values, exploiting the parallel performance of the developed method (Cifani et al., 2018).

Recently, Santarelli and Fröhlich (2015, 2016) considered up to 2880 spherical bubbles in a larger channel. In these studies the bubbles were treated as rigid spheres and a uniform mass density in the governing equations was assumed, simplifying the problem. Here, we steer away from such simplifications while retaining $\mathcal{O}(10^3)$ deformable bubbles in a full-scale channel flow treated in full DNS detail.

Among the two possible configurations for vertical channel flows, i.e., upflow and downflow, we focus on the latter. The reason is twofold. First of all, research in the past has mainly been focused on upflow configurations. Moreover, studies that do concern downflow configurations report a lower Reynolds number, limited domain size and smaller range of bubble sizes. Secondly, an important feature of bubble-laden downflow is the accumulation of bubbles in the core of the channel, which has the effect of increasing the homogeneity of flow features compared to single-phase channel flow. This offers a compelling opportunity to compare simulation results with homogenous bubbly flow studies involving pseudo-turbulence, both numerically (Bunner and Tryggvason, 2002a; 2002b; Roghair et al., 2011) and experimentally (Mercado et al., 2010). Furthermore, liquid kinetic energy spectra in channel core will be compared with those obtained in very recent experiments (Prakash et al., 2016), in which bubbles were injected into approximately homogeneous isotropic turbulence. In view of these reasons, our study extends the earlier investigations on downflow and provides robust statistical data for the validation of turbulent bubble-laden flow models.

The paper is structured as follows. In Section 2 the problem definition and numerical approach will be described. A short introduction of the governing equations and the employed numerical methods will be given in Section 2.1. The description of the simulations and the choice of parameters is given in Section 2.2. Simulation findings are gathered in Section 3. Liquid flow statistics are collected and analysed in Section 3.1. Subsequently, the bubbles microstructuring is investigated in Section 3.2. Moreover, the probability density functions of bubble velocity fluctuations and the scaling of the liquid kinetic energy spectra are analysed in Section 3.3 and Section 3.4, respectively. Finally, the main findings and an overview of possible future developments are provided in Section 4.

2. Problem definition and numerical approach

In this section we present the governing equations and numerical method in Section 2.1 and discuss the set-up of the simulated cases in Section 2.2.

2.1. Governing equations and discretisation methods

The mathematical model used for resolved bubble-laden flows is based on the so called "one-fluid formulation" of the governing equations (Prosperetti and Tryggvason, 2007). A single set of equations is solved for the whole field with differences in the material properties and interfacial terms (e.g., surface tension) accounted for with the help of a marker function *f*. The non-dimensional incompressible Navier-Stokes equation and continuity equation are used for the simulation of the turbulent flows:

$$\rho\left[\frac{\partial \mathbf{u}}{\partial t} + \nabla\cdot(\mathbf{uu})\right] = -\nabla p + \frac{1}{Fr^2}(\rho-\rho_0)\hat{\mathbf{g}} + \frac{1}{Re}\nabla\cdot(2\mu\mathbf{D}) + \frac{1}{We}k\mathbf{n}\delta(n), \tag{1}$$

$$\nabla\cdot\mathbf{u} = 0, \tag{2}$$

where $\mathbf{u}$ is the velocity, p the pressure, t the time, k the curvature of the interface between gas and liquid, $\mathbf{n}$ the normal vector to the interface, $\mathbf{D}$ the deformation tensor, $Fr = u/\sqrt{gL}$ the Froude number with L a reference length, $Re = UL/\nu_l$ the Reynolds number with U a reference velocity and $\nu_l = \mu_l/\rho_l$ the kinematic viscosity of the liquid in terms of the liquid's dynamic viscosity μ_l and liquid mass density ρ_l. Moreover, $We = LU^2\rho_l/\sigma$ is the Weber number with surface tension of the bubble interface σ. Throughout, the domain ρ and μ are respectively the non-dimensional mass density and dynamic viscosity defined as

$$\rho = 1 \cdot (1 - f) + \frac{\rho_g}{\rho_l} f, \tag{3}$$

$$\mu = 1 \cdot (1 - f) + \frac{\mu_g}{\mu_l} f, \tag{4}$$

where ρ_g, μ_g are the mass density and the dynamic viscosity of the gas phase, respectively. The additional force $-\frac{1}{Fr^2}\rho_0 \hat{\mathbf{g}}$ balances the weight of the mixture (Bunner and Tryggvason, 2002a), which leads to $\rho_0 = \frac{1}{V}\int \rho dV$ with V the volume of the domain.

In the presence of more than one bubble, an individual marker function f_i is assigned to each bubble, with $f_i = 1$ wherever bubble i is located and $f_i = 0$ elsewhere. Given N bubbles, an equal number of hyperbolic equations is solved:

$$\frac{\partial f_i}{\partial t} + \mathbf{u} \cdot \nabla f_i = 0 \qquad i = 1, \ldots, N. \tag{5}$$

This formulation, referred to as multiple-marker formulation (Coyajee and Boersma, 2009), introduces a convenient numerical setting to account for bubble-bubble interaction and avoid numerical coalescence. According to (Coyajee and Boersma, 2009) the global volume fraction f is derived from the individual markers f_i as $f = \max(f_i)$. Whenever two or more interface segments lie within the same computational cell the total contribution of the surface tension will be the sum of the individual surface tension terms. Before the total surface tension term in Eq. (1) is assembled, curvature and interface normal are computed from the single marker functions. This is an advantage of the multiple-marker formulation, which allows to reconstruct the geometry of closely interacting bubbles from separate f_i and hence avoid inaccuracy otherwise present if the geometry would be deduced from the locally combined f. In Kwakkel et al. (2013) the multiple-marker formulation has been employed to simulate collisions and breakups in droplet-laden flows. While the dynamics of the film between impacting droplets is unresolved, the overall dynamics of the droplets is well captured and a good agreement with experimental studies has been obtained for bouncing, merging and near head-on separating collisions. Similarly, in Cifani et al. (2018) a grid convergence study has been conducted on a head-on collision of droplets revealing close to theoretical convergence rate. Moreover, an overlapping region of the two marker functions limited to about one grid cell was found in all simulated resolutions. This gives confidence that the multiple-marker formulation is suitable for flows where bouncing collisions are relevant. The latter is the regime that we seek to analyse in this work.

Eqs. (1)–(5) are numerically solved by employing the massively parallel code detailed in Cifani et al. (2018). The latter solver has been specifically designed to efficiently handle wall-bounded turbulent bubbly flows loaded with a large number of deformable bubbles. The time marching of the momentum equation is carried out by a fully explicit second-order Adams-Bashforth (AB2) scheme (Wesseling, 2009). The discrete fields are arranged on a staggered grid. The velocity components are defined at the cell faces while the pressure field and the volume fraction fields are defined at the cell centres. The convective term $\nabla \cdot (\mathbf{uu})$ is discretised in a second-order energy conserving form, as described in Vreman (2014). The pressure and viscous term are discretised by standard second-order central finite differences. The values of density and viscosity needed at the cell faces are linearly interpolated from the cell centres. The surface tension is mapped onto the Eulerian grid by means of the volume fraction gradient in such a way that a discrete balance between ∇p and ∇f (Francois et al., 2006; Popinet, 2009; 2018) is obtained. For a staggered grid this simply corresponds to standard finite-differences across a cell face. For example, the x-component of the volume fraction gradient will be $\left(f_{i+1,j,k} - f_{i,j,k}\right)/h_{c,i}$ where i, j, k indicates a control volume and $h_{c,i}$ is the grid spacing between node $i+1$ and i. An accurate curvature computation of the bubbles is achieved by using the Generalised Height Function method (Popinet, 2009; Cifani et al., 2018).

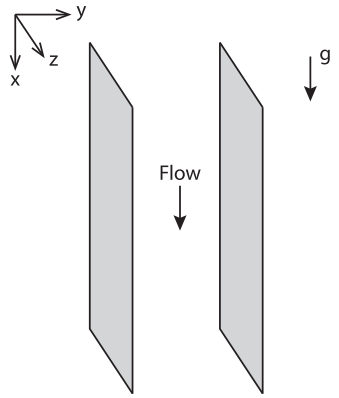

Fig. 1. Sketch of the downflow channel configuration used in this paper.

The transport of f, being the volume fraction in the VOF method, is carried out by a geometrical reconstruction algorithm (Cifani et al., 2016) which ensures sharpness of f throughout the entire simulation time. The multiple-marker formulation requires the advection of N hyperbolic equations as in Eq. (5). In order to limit computational time and memory usage, each marker function f_i is solved on a local rectangular box that fits around the bubble and moves along with it. The details of the computational performance of the VOF solver are provided in Cifani et al. (2018).

Continuity equation Eq. (2) leads to a Poisson equation for pressure with variable coefficients given by the inverse of density. However, the same equation can be transformed into a constant-coefficient Poisson equation, which makes it possible to use fast Poisson solvers (Dodd and Ferrante, 2014). The semi-discrete form of the pressure equation then reads:

$$\nabla^2 p^{n+1} = \nabla \cdot \left[\left(1 - \frac{\rho_g}{\rho^{n+1}}\right)\nabla \hat{p}\right] + \nabla \cdot \left(\rho_g \frac{\mathbf{u}^*}{\Delta t}\right) \tag{6}$$

where $\nabla \hat{p}$ is an approximation of $\nabla \hat{p}^{n+1}$ and $\mathbf{u}^*$ the discrete velocity field computed from Eq. (1). Particular care has to be taken when discretising the pressure derivatives in Eq. (6) since the pressure field is discontinuous across the two-phase interface due to surface tension. In particular, as shown in Cifani (2019), by appropriately combining the extrapolated pressure gradient with a matching volume fraction an accurate numerical solution at high density ratios can be achieved. This is also the method employed in this work.

2.2. Case definition

The domain of interest, sketched in Fig. 1, is a vertical channel of size $L_x = 4\pi H$, $L_y = 2H$ and $L_z = 4/3\pi H$, where x, y, z are the stream-wise, the wall normal and the span-wise directions, respectively. The size parameter H equals 1. The direction of gravity is aligned with the stream-wise direction, hence configuring a downflow. Periodic boundary conditions are applied along the

stream-wise and the span-wise directions, while no-slip boundaries are applied at the two walls. The flow is driven by a pressure gradient, which is dynamically adjusted in order to keep the volumetric flow rate constant. The bulk Reynolds number Re_{2H} based on the channel height and the average liquid velocity is approximately 6300.

Starting from the velocity field of a fully developed single-phase turbulent channel flow, three different gas volume fractions are simulated until an approximate statistically steady state is reached. In particular, gas volume fractions of $\alpha = 0.5\%$, $\alpha = 2.5\%$ and of $\alpha = 10\%$ are considered corresponding to a number of bubbles $N_b = 64$, $N_b = 320$ and $N_b = 1280$, respectively. The bubbles, fully deformable, are of equal size and initialised as spheres of diameter $D = H/4$. Here, we are interested in the statistically steady state, which is independent of the initial bubble distribution. This was numerically verified in Cifani (2017) where two different initial arrays composed of the same number of bubbles were evolved in time until a statistically steady state. Both cases were found to yield the same flow statistics. The average bubble Reynolds number varies, depending on the gas volume fraction, from $Re_b = 160$ for the most dilute case to $Re_b = 90$ for the most dense case. The latter, together with the Eötvös number, $Eo = \rho_l g D^2/\sigma = 0.67$, places the bubble deformability in the nearly spherical/ellipsoidal range (Grace, 1973). This physically prevents break-ups and the formation of small satellites. However, events of bubble coalescence, depending on flow conditions, may still be present and could influence the bubble size distribution at statistically steady state. Numerically, this can be accounted for by assigning an additional marker function to the newly formed agglomerate of bubbles, as detailed in Kwakkel et al. (2013). In this work coalescence is numerically prevented. Finally, the density ratio ρ_l/ρ_g and the dynamic viscosity ratio μ_l/μ_g have been set to 20.

The choice of the material properties requires additional explanation. High density and viscosity ratios are numerically demanding, often leading to extreme grid refinements around the two-phase interface in order to avoid large numerical errors. Preliminary results showed that, for high ρ_l/ρ_g and μ_l/μ_g, in the event of bubble collisions unphysical velocities, confined to a few grid cells, appear around the bubble interface, hinting at an unresolved velocity field on the available grid. The dynamics of dispersed light objects (as in bubbly flows) is, however, mainly dictated by the forces transferred from the liquid phase to the interface. At high density and viscosity ratios ($\gtrsim 50$), the contribution to these forces exerted by the gas phase becomes negligible (Bunner and Tryggvason, 2002a). This suggests that for the present choice of material properties the bubble motion is dominated by the liquid flow.

The computational domain is discretised by $n_x = 1152$, $n_y = 240$ and $n_z = 384$ evenly spaced grid points along each direction. This corresponds to a grid size, scaled by the wall unit, equal to $\Delta x^+ = 1.96$, $\Delta y^+ = 1.48$ and $\Delta z^+ = 2.16$. These resolution characteristics ensure a well resolved bubble shape over the whole domain, with approximately 25 grid points per bubble diameter (Cifani et al., 2018). Simulation of a single-phase channel flow, at the same resolution in terms of wall units, has been carried out in Cifani et al. (2018) and compared against an independent and well established spectral method (Vreman and Kuerten, 2014). First and second order statistics of the velocity field were obtained with a maximum relative error around 1%. As for the resolution required by the flow and wakes around the bubbles, a point of reference can be found in Lu and Tryggvason (2006) where an average of 16 grid points per bubble diameter were used for approximately the same Re_b simulated here. Additionally, the grid refinement study carried out in Uhlmann (2008) for rigid spheres at $Re_b = 136$ showed an error of about 7% for second-moment fluid statistics when comparing results with ≈ 13 grid points per diameter with those from ≈ 26 grid points per diameter. Since we concentrate on bubbles with nearly spherical/ellipsoidal shape, these findings confirm the adequateness of the employed resolution for the quantities of interest in this paper.

3. Flow statistics, bubble structures and spectral properties

In order to gain insight in the modulation of turbulence by the presence of a dispersed gas phase as well as to understand bubble motion and microstructure, a number of Eulerian and Lagrangian quantities have been gathered in the statistically steady-state regime. The results are divided into two groups. The first group, presented in Section 3.1, is concerned with first and second order statistics of the liquid velocity. These quantities have been averaged over a period of $T = 20H/u_\tau$ for volume fractions $\alpha = 0.5\%, 2\%$ and over a period of $T = 13H/u_\tau$ for volume fraction $\alpha = 10\%$. Here, u_τ is the friction velocity. This corresponds to approximately 27 and 18 flow-through times of the selected channel, respectively.

A second set of quantities, aimed to understand bubble clustering, preferential direction of alignment, probability density functions of the bubble velocity as well as scaling of the kinetic energy spectra is reported in Sections. 3.2–3.4. These quantities have been post-processed for a period $T = 5H/u_\tau$ with a sampling rate $\Delta t_s = 1 \cdot 10^{-2} H/u_\tau$, corresponding to approximately a distance of $0.14D$ travelled by a bubble in time Δt_s with respect to the surrounding liquid. The statistical convergence of the latter results is shown in Appendix A.

3.1. First and second-order fluid statistics

A measure of the proximity of the flow to a statistically steady state is the average wall shear stress τ_w, which balances the total weight of the mixture and the imposed driving force (Lu and Tryggvason, 2006). Fig. 2 shows the total shear stress as a function of time for different gas volume fractions. The statistics of the densest case ($\alpha = 10\%$), collected for a period $T = 13H/u_\tau$, were found to converge faster than those related to the more dilute flows. For very low gas volume fractions, due to random velocity fluctuations, bubbles may tend to reside longer at a certain wall-normal coordinate $\bar{y}$ compared to its symmetric position $2H - \bar{y}$. In order to ensure well converged average profiles, the simulations for $\alpha = 0.5\%$ and $\alpha = 2.5\%$ were carried out for a longer period equal to $20H/u_\tau$.

For $\alpha = 0.5\%$ and $\alpha = 2.5\%$ the shear stress at the wall is on average close to the value of the corresponding single-phase flow. Remarkably, for $\alpha = 10\%$ an increase of τ_w of about 17% is observed. In order to investigate the effect of buoyancy on τ_w we have performed an additional simulation at $\alpha = 10\%$ where gravity was numerically set to zero. An increase of τ_w approximately equal to that measured for the buoyant case was observed. This suggests that, in this setup, τ_w increases mainly due to the stirring of the bubbles, which penetrates deeper into the near wall region with increasing volume fractions (see the mean volume fraction profile of Fig. 3).

The statistics of the liquid phase can be computed by appropriately sampling the velocity field based on the volume fraction values. To this end, the definition used in Cifani et al. (2018) and reported here for completeness is employed:

$$< q >= \frac{\overline{c \cdot q}}{\overline{c}}, \tag{7}$$

$$rms(q')_c = \sqrt{\frac{\overline{cq^2}}{\overline{c}} - \left(\frac{\overline{cq}}{\overline{c}}\right)^2}, \tag{8}$$

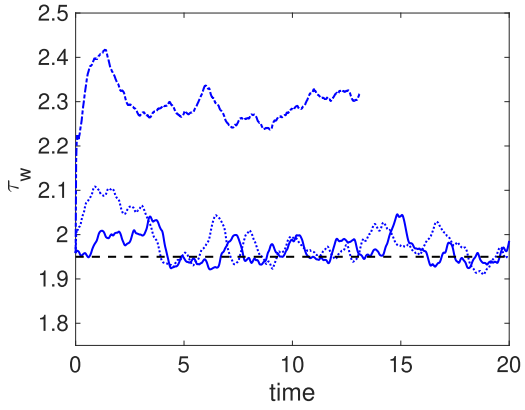

Fig. 2. Total instantaneous wall-averaged shear stress as a function of time for $\alpha = 0.5\%$ (solid line), $\alpha = 2.5\%$ (dotted line) and $\alpha = 10\%$ (dash-dotted line). τ_w of the corresponding single-phase flow at $t = 0$ is reported by the dashed black line.

where $c = 1 - f$, q is the quantity of interest, q' its fluctuation, and $\overline{(\cdot)}$ indicates the average over time and the homogenous directions. In Fig. 3 the mean volume fraction and the mean stream-wise velocity $< u >$ are shown for different α. The profiles have not been averaged over the two halves of the channel, as in Lu and Tryggvason (2006), but the profiles over the entire height of the channel are shown. The high degree of symmetry observed, even for the smallest number of bubbles, is indicative of well-converged statistical quantities.

Clearly, the bubbles tend to accumulate in the core of the channel. According to Lu et al. (2006) this phenomenon is caused by the lift force exerted on the bubbles. As α increases to 10%, $\overline{f}$ becomes approximately constant from $y = 0.5$, while showing a characteristic peak in the transition from the near-wall region to the core. This same trend was also shown in Lu and Tryggvason (2006) for $\alpha = 6\%$, for a smaller channel and lower Re. As for $< u >$, no significant differences are present for $\alpha = 0.5\%$ with respect to the single-phase flow. When the gas volume fraction equals $\alpha = 10\%$ a clear uniform velocity region is formed within the same range of the plateau shown by $\overline{f}$. The mean shear becomes zero at equilibrium, preventing the lateral migration of the bubbles (Lu et al., 2006; Lu and Tryggvason, 2006).

Fig. 4 shows the rms of u', the rms of v' and the rms of w'. The stream-wise velocity fluctuations for $\alpha = 0.5\%$ and $\alpha = 2.5\%$ adhere closely to the corresponding single-phase velocity fluctuations up to $y = 0.15$. Beyond this point a gradual decrease for the case of $\alpha = 2.5\%$ is observed until reaching an approximately constant value of about 1.0, which is about 1.2 times higher than the level of single-phase velocity fluctuation at the center line. The deviation from the single-phase profile for the case of $\alpha = 10\%$ is much stronger and starts close to the wall around $y = 0.03$. The peak is reached at $y = 0.08$, i.e., at approximately the same location as the corresponding single-phase profile. However, the maximum, equal to 1.9, is about 1.4 times lower for $\alpha = 10\%$. In addition, an approximate constant value, slightly higher than that of $\alpha = 2.5\%$, is observed from $y = 0.42$.

The introduction of a significant number of bubbles generates a homogeneous region in the core of the channel, which broadens as α increases. For the highest gas concentration analysed a strong turbulent intensity reduction is observed close to the wall. The wall-normal velocity fluctuations, reported in Fig. 4, show a decreasing intensity for $\alpha = 0.5\%$ for all values of y. At the highest gas volume fraction, however, a value of about 1.3 times larger than that of the corresponding single-phase flow is reached in the core of the channel. Turbulence attenuation at the wall is also clearly visible. Analogous considerations apply to the rms of w'.

3.2. Bubble distribution

The formation of preferential clustering and dominant directions of alignment within the flow can be analysed by means of the pair probability distribution function $G(r, \theta)$, defined as (Bunner and Tryggvason, 2002a)

$$G(r,\theta) = \frac{V}{N_b(N_b-1)}\left\langle \sum_{i=1,N_b} \sum_{j=1,N_b i\neq j} \delta(\mathbf{r} - \mathbf{r}_{ij}) \right\rangle, \tag{9}$$

which states the probability of the distance vector $\mathbf{r}_{ij}$ between the centroids of two bubbles i and j having norm r and forming an angle θ with respect to a reference direction. The latter is chosen to be equal to the stream-wise direction. In (9), V is the volume containing N_b bubbles. In wall bounded flows $G(r, \theta)$ is, in general, also a function of the wall-normal coordinate. However, as illustrated in Section 3.1, with α increasing a fairly homogeneous region forms in a large part of the bulk of the channel where the gas volume fraction is essentially independent of y. Even for the dilute case the bubbles are concentrated in the core region. Thus, we investigate the dependency of the pair probability distribution function only on r and θ, making the analysis directly comparable with pseudo-turbulent studies (Bunner and Tryggvason, 2002a). This is also the choice of Santarelli and Fröhlich (2015).

The radial pair distribution function $G(r)$, shown in Fig. 5, is obtained by integrating (9) over a thin shell of width Δr and radius r.

For randomly distributed bubbles $G(r)$ equals one. However, due to the lack of bubbles in those sampling volumes whose boundaries exceed the walls, $G(r)$ deviates from 1 decreasing with r. For this reason, as a point of reference, the radial distribution function of 1280 randomly distributed bubbles averaged over 500 samples has been included in Fig. 5. Moreover, the maximum sepa-

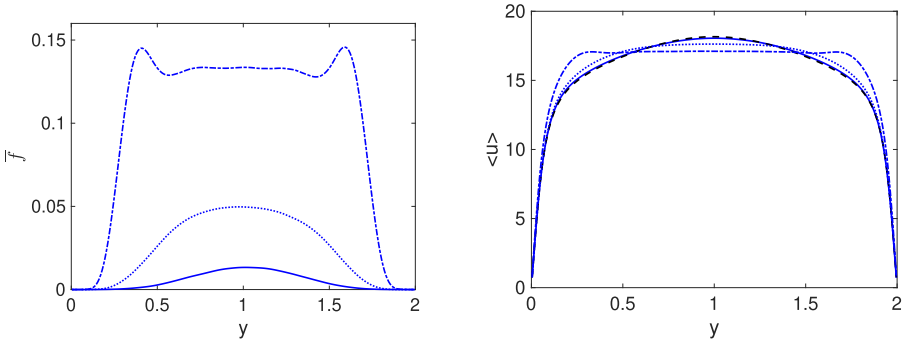

Fig. 3. Average gas volume fraction field (left panel) and average stream-wise velocity (right panel) as a function of the wall-normal coordinate. The line legend is the same as in Fig. 2. The dashed black line in the right panel is the mean velocity profile for the corresponding single-phase flow.

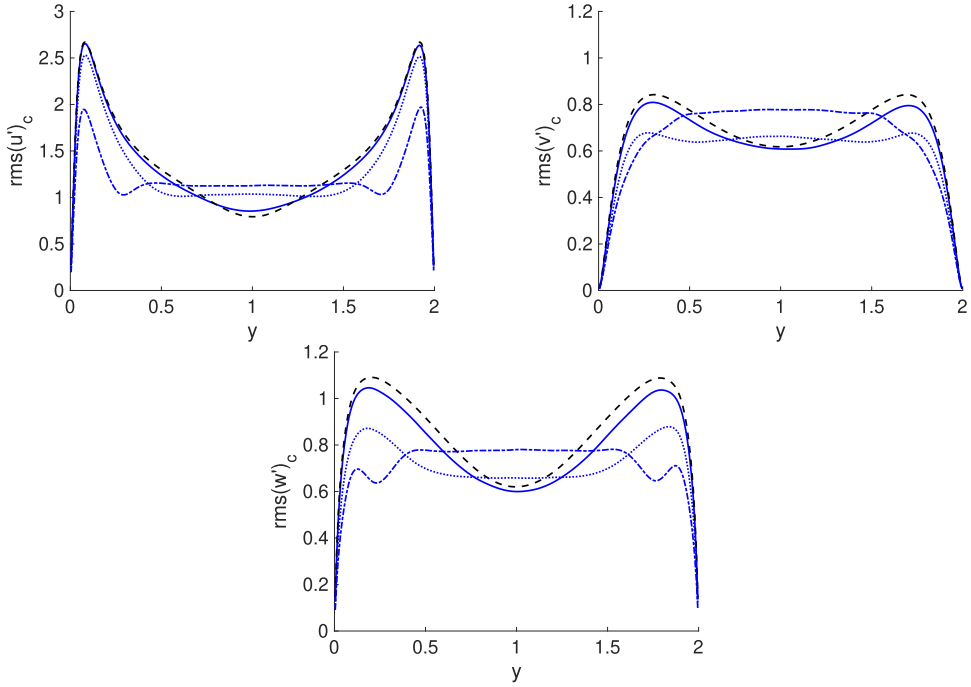

Fig. 4. Second order velocity statistics, normalised by the friction velocity, as a function of the wall normal coordinate for different α: rms of the stream-wise velocity fluctuations (left-top panel), rms of the wall-normal velocity fluctuations v' (right-top panel), rms of the span-wise velocity fluctuations w' (bottom panel). The line legend is the same as in Fig. 3.

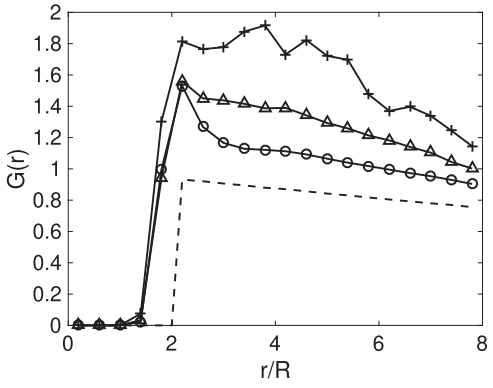

Fig. 5. Radial pair distribution as a function of the scaled radius r/R, with R the bubble radius, for $\alpha = 0.5\%$ (line with crosses), $\alpha = 2.5\%$ (line with triangles), $\alpha = 10\%$ (line with circles). The same quantity for randomly distributed bubbles is represented by the dashed line.

ration distance investigated has been limited to H (Santarelli and Fröhlich, 2015). Given the deformability of the bubbles, $G(r) > 0$ for $r/R < 2$. The latter holds true also for $\alpha = 0.5\%$ indicating the occurrence of a significant amount of bubble collisions also for the most dilute case. Remarkably, a maximum is observed at $r/R = 2.2$ independent of the gas volume fraction investigated, which indicates the presence of agglomeration of bubbles at small separation distances.

The formation of localised clusters is also qualitatively visible from the snapshots reported in Fig. 6. This tendency for bubbles to attract each other is well documented (Bunner and Tryggvason, 2002a). According to potential flow theory, the pressure inside the gap between two bubbles is lower than the surrounding pressure driving the bubbles to collide. An additional attractive effect is given by the bubble wakes. A bubble in the wake of another upstream bubble tends to move towards the latter. Experiments conducted at similar Re_b for in-line air-bubbles have shown the same attractive behaviour (Katz and Meneveau, 1996).

For $\alpha = 0.5\%$ subsequent peak is observed at $r/R = 3.8$, hinting at a longer range bubble interaction. On the contrary, for the higher gas volume fractions $G(r)$ monotonically decreases towards the random distribution profile. Noticeable differences arise with studies on pseudo-turbulence conducted by Bunner and Tryggvason (2002a). In their results, at $\alpha \approx 2\%$ the close distance peak at $r/R = 2.2$ is absent. Furthermore, the peaks at the corresponding gas volume fractions are shifted towards larger r. In down-flow channel configurations, the additional effect of the lift force, which drives the bubbles towards the core, could explain the enhanced clustering even at the lowest values of simulated α. As the gas volume fraction increases, however, the profile of $G(r)$ approaches that of pseudo-turbulence with a sharp decay after the maximum and a close to random distribution for $r/R > 4$.

The angular pair distribution, $G(\theta)$, is constructed by integrating (9) along the azimuthal direction of a spherical sector between radius $r - \Delta r$ and $r + \Delta r$ having angular width $\Delta\theta$. The resulting profiles, shown in Fig. 7, have been normalised so that $\int_0^1 G(\theta')d\theta' = 1$, with $\theta' = \theta/\pi$, as reported in the experimental results (Mercado et al., 2010).

At small distances a strong horizontal alignment is observed for all examined gas volume fractions, also qualitatively visible from Fig. 6. At $r/R = 2.5$ the maximum peak around $\theta = \pi/2$ decreases as α increases. At longer distances $G(\theta)$ approaches 1, meaning that the bubbles are approximately randomly distributed. However, as r increases a tendency for vertical alignment appears, which was not found in the studies of homogeneous bubbly flow (Bunner and Tryggvason, 2002a). This behaviour is more pronounced for $\alpha = 0.5\%$, adhering more closely to the experimental studies (Mercado et al., 2010). As for the radial pair distribution, significant differences are present for the intermediate gas concentration $\alpha = 2.5\%$ with respect to the findings of Bunner and Tryggvason (2002a). At $r/R = 4$, $G(\theta)$ is essentially uniform and close to 1, while in Bunner and Tryggvason (2002a) a strong horizon-

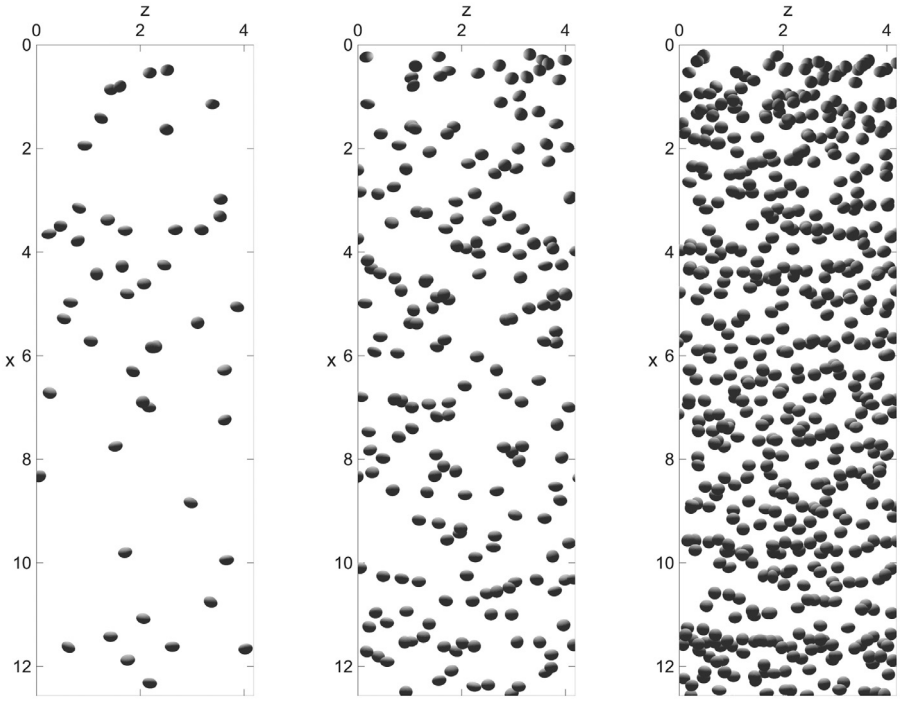

Fig. 6. Isosurfaces of $f = 0.5$ in the developed statistically steady state of bubbles located at $0.7H \leq y \leq 1.3H$ for $\alpha = 0.5\%$ (left panel), $\alpha = 2.5\%$ (center panel) and for $\alpha = 10\%$ (right panel).

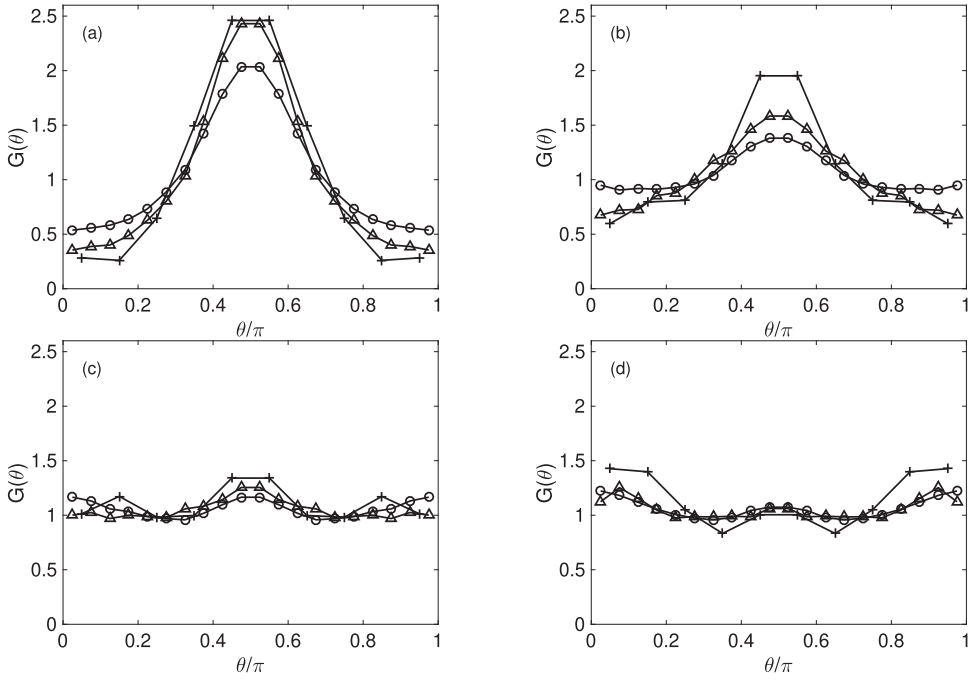

Fig. 7. Angular pair distribution function at $r/R = 2.5$ (a), $r/R = 3$ (b), $r/R = 4$ (c), $r/R = 5$ (d) as a function of θ/π. The lines with crosses correspond to $\alpha = 0.5\%$, the lines with triangles correspond to $\alpha = 2.5\%$, the lines with circles correspond to $\alpha = 10\%$.

tal alignment is still present. The absence of large horizontal rafts, typically formed by a swarm of buoyant bubbles at high values of α, can be related to the interaction with the underlying turbulence generated by the channel flow, which would tend to disrupt large horizontal structures. A confirmation of the influence of turbulence on the bubbles motion is given by the probability density functions of the bubble velocity reported in Figs. 11 and 12. The latter are in good agreement with the normal distribution. On the contrary, significant deviation from the Gaussian distribution have been reported for pseudo-turbulence, both numerically (Bunner and Tryggvason, 2002a) and experimentally (Mercado et al., 2010).

The mechanisms of attraction and repulsion can studied by analysing the relative velocity of bubble pairs. Following the methodology used in Bunner and Tryggvason (2002a), we look at the probability of the relative radial velocity V_r and the tangential velocity V_θ of being positive. The latter is defined as the meridian component of the relative velocity in a spherical coordinate system as shown in Fig. 8.

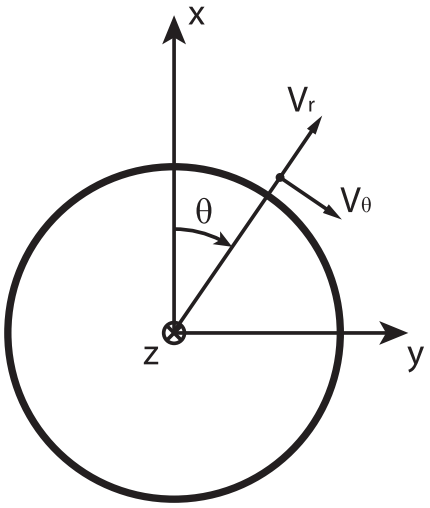

Fig. 8. Sketch of positive relative radial velocity V_r and the tangential velocity V_θ at a given meridian angle θ. The circle represents the surface of a reference bubble.

$P(V_r > 0)$ is shown in Fig. 9.

A tendency to mild repulsion is observed at all investigated α around $\theta = \pi/2$, analogously to the findings of Bunner and Tryggvason (2002a). As $\theta \to \pi$ a reversed behaviour is in general observed, with attraction being more likely than repulsion. At high gas volume fractions however, the dependency of $P(V_r > 0)$ on the various angular positions for $r/R \geq 4$ is rather weak and V_r can be considered, in first approximation, to have equal probability of being positive or negative.

In the study of two vertically aligned spherical bubbles (Yuan and Prosperetti, 1994) two effects were identified to influence the relative motion of the bubbles. A first contribution is due to the wake effect which drives the bubbles to collide and a second contribution is due to inertial effects which tend to push the bubbles apart. The former is dominant at long separation distances, the latter is dominant at small separation distances. Hence, an equilibrium value of r can be found. According to Yuan and Prosperetti (1994), for our study this value ranges from $4R$ to $5R$, which would result in a repulsive behaviour at practically all investigated r. A tendency to repulsion is indeed observed for the very dilute case at $\theta = \pi$. Nevertheless, the system investigated here is substantially different from the test case of two symmetric bubbles analysed by Yuan and Prosperetti (1994). The combined presence of turbulence and the interaction between multiple bubbles appears to largely reduce the correlation of the motion of bubble pairs for $r/R > 4$.

Fig. 10 shows $P(V_\theta > 0)$ as a function of θ at the same radii analysed for $P(V_r > 0)$.

At close distances, $P(V_\theta > 0)$ is higher than 0.5 for $\theta < \pi/2$ and lower than 0.5 for $\theta > \pi/2$, for $\alpha = 2.5\%$ and $\alpha = 10\%$. This indicates the tendency of bubbles to rotate from a given θ towards horizontal alignment, consistently with the findings observed for $G(\theta)$ (Fig. 7). As r increases, $P(V_\theta > 0)$ tends to 0.5 independently of θ with virtually no correlation for $r/R > 3$. At close distances, for $\alpha = 0.5\%$ there is an inversion of behaviour with $P(V_\theta > 0) < 0.5$ indicating that two bubbles are more likely to rotate around each other towards the poles ($\theta = 0, \pi$). Nonetheless, the latter trend is confined to a small spherical sector and, as such, less probable with respect to horizontal alignment.

3.3. Pdf of bubble velocity fluctuations

We next quantify the bubble motion in terms of the probability density function (pdf) of the bubble velocity fluctuations. The bubble velocities are calculated by using the individual marker functions. For example, the bubble velocity along the stream-wise direction is computed as

$$U_i = \frac{1}{V_b} \int_V f_i u \, dV \tag{10}$$

with U_i the velocity of bubble i and V_b its volume. The span-wise and the wall-normal bubble velocity are defined analogously.

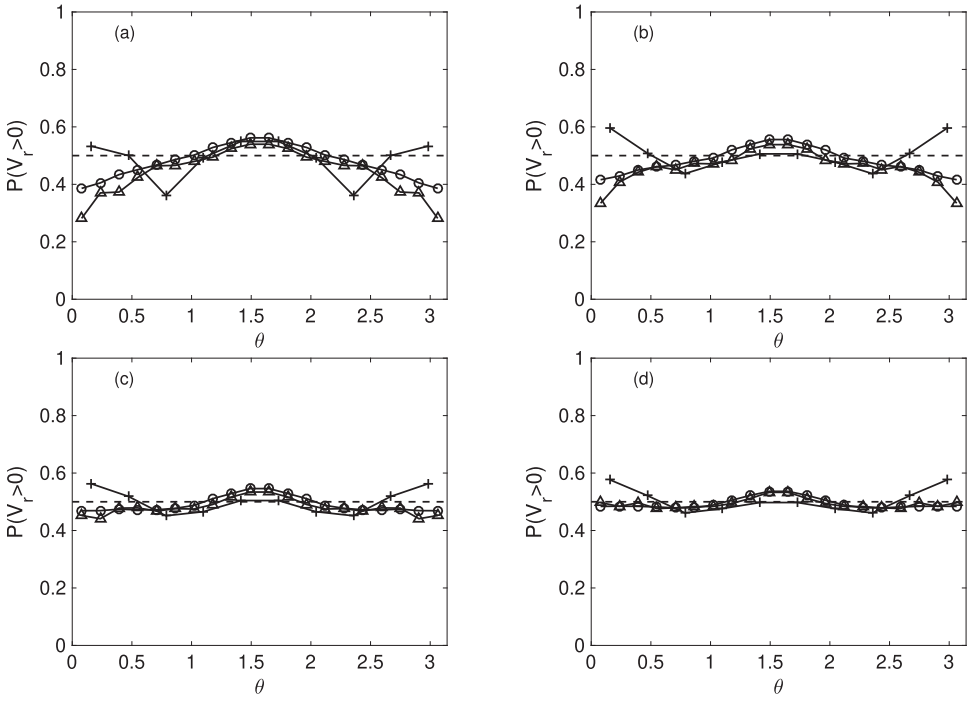

Fig. 9. $P(V_r > 0)$ at $r/R = 2.5$ (a), $r/R = 3$ (b), $r/R = 4$ (c), $r/R = 5$ (d) as a function of θ. The lines with crosses correspond to $\alpha = 0.5\%$, the lines with triangles correspond to $\alpha = 2.5\%$, the lines with circles correspond to $\alpha = 10\%$. The dashed lines indicate probability equal to 0.5.

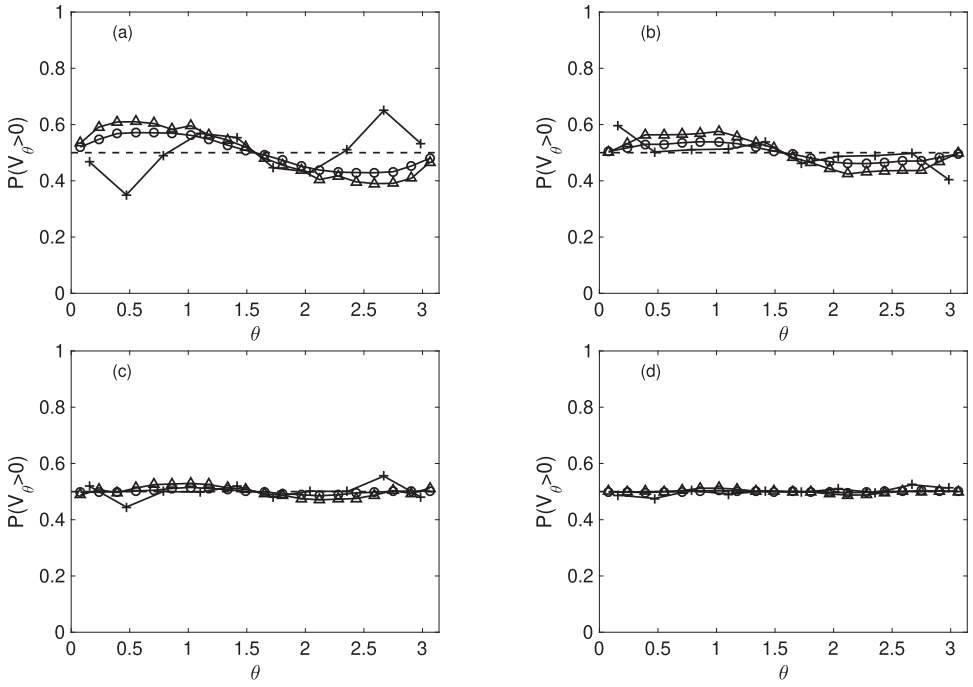

Fig. 10. $P(V_\theta > 0)$ at $r/R = 2.5$ (a), $r/R = 3$ (b), $r/R = 4$ (c), $r/R = 5$ (d) as a function of θ. The line with crosses correspond to $\alpha = 0.5\%$, the lines with triangles correspond to $\alpha = 2.5\%$, the lines with circles correspond to $\alpha = 10\%$. The dashed lines indicate probability equal to 0.5.

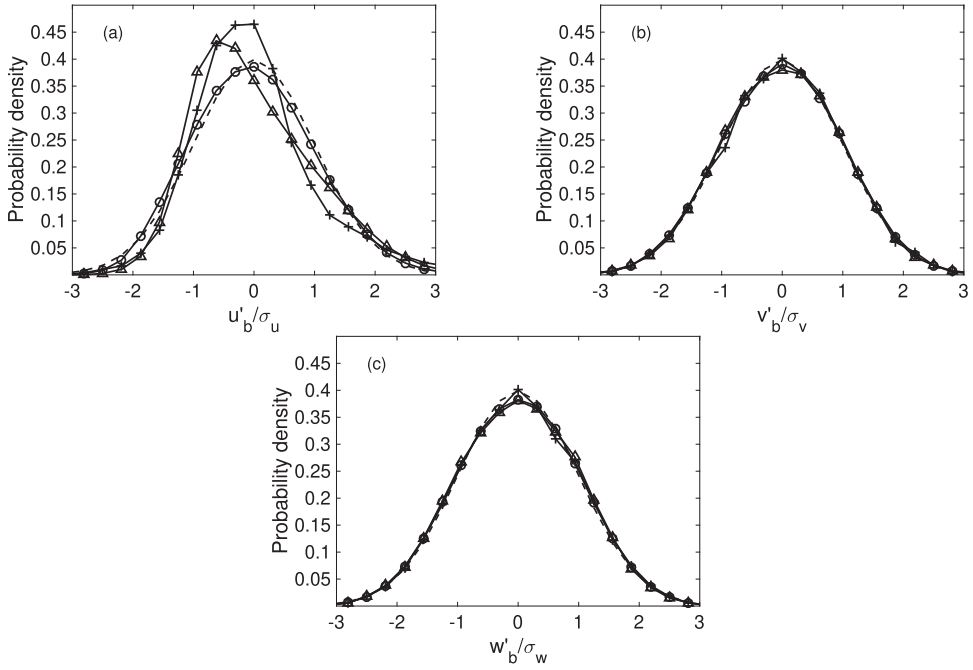

Fig. 11. Probability density functions of the bubble velocity fluctuations u_b' (a), v_b' (b) and w_b' (c) normalised by their standard deviation σ_u, σ_v and σ_w, respectively. The lines with crosses correspond to $\alpha = 0.5\%$, the lines with triangles correspond to $\alpha = 2.5\%$, the lines with circles correspond to $\alpha = 10\%$. The dashed lines indicate the Gaussian distribution.

Fig. 11 shows the stream-wise, wall-normal and span-wise bubble velocity fluctuations indicated by u_b', v_b', w_b' and normalised by their standard deviation σ_u, σ_v and σ_w, respectively. The pdf of the Gaussian distribution is also reported for comparison.

The distributions of v_b' and w_b' tend to closely adhere to the Gaussian as the gas volume fraction increases, being well approximated by the normal distribution even for the most dilute case investigated. The velocity fluctuations along the stream-wise direction are asymmetric with a mean value shifted towards negative values. At $\alpha = 0.5\%$ a maximum of about 0.46 is reached between $-0.3 \leq u_b'/\sigma_u < 0$. At $\alpha = 10\%$ the profile regains symmetry closely matching the Gaussian. The predominance of a rise velocity lower than the mean has been explained by Bunner and Tryggvason (2002b) as the result of preferential horizontal clusters (also confirmed by our results on channel flow of Fig. 7) characterised by lower drift velocity than the average. However, the pdf pro-

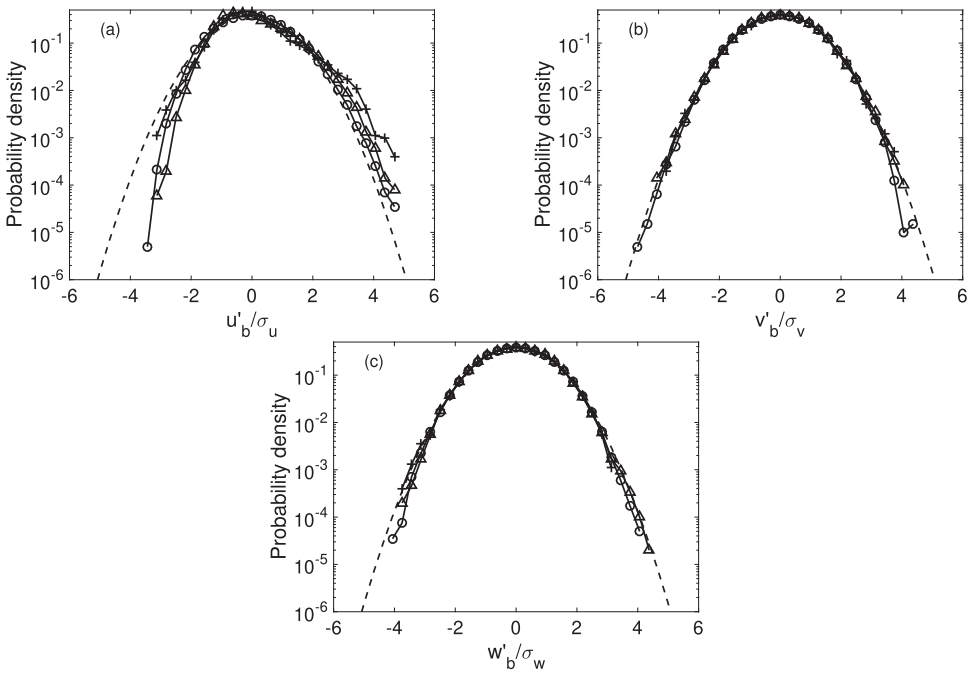

Fig. 12. Probability density functions of the bubble velocity fluctuations u_b' (a), v_b' (b) and w_b' (c) normalised by their standard deviation σ_u, σ_v and σ_w, respectively. A semi logarithmic scale has been used. The description of the lines is the same as in Fig. 11.

files reported here appear to match more closely the normal distribution, especially at higher α, whereas in Bunner and Tryggvason (2002b) significant differences are reported also at high gas volume fractions.

In order to highlight the behaviour of the tails of the pdf we present in Fig. 12 the same results as in Fig. 11 in a semi logarithmic scale.

The pdf of u_b' appears to significantly differ from a Gaussian distribution in the tails for $|u_b'/\sigma_u| > 2$ with predominant positive fluctuations. The pdf's of v_b' and w_b' can in good approximation be considered Gaussian. This is in neat contrast with the pdf of pseudo-turbulence (Mercado et al., 2010), which show non-Gaussian tails. Thus, the difference reported here is attributed to the interaction with the bubble motion and the base turbulence supplied by the channel flow. This could also explain the differences observed in Fig. 11 with the findings of Bunner and Tryggvason (2002b).

3.4. Liquid kinetic energy spectrum

The motion of large-sized bubbles strongly influences the kinetic energy spectrum by generating what in the pioneering work of Lance and Bataille (1983) has been referred to as pseudo-turbulent perturbations. A modification of the behaviour in the high-frequency range has been observed, with the progressive replacement of the Kolmogorov energy cascade mechanism by a $-8/3$ power law (Lance and Bataille, 1983). In the same work, it was argued that the kinetic energy can be estimated from the dissipation rate being a fraction of the work exerted by the drag force experienced by the bubbles. This, together with the observation that the eddies related to the bubble wakes dissipate before fragmenting into smaller scales, led to a -3 scaling. Since then, the latter scaling has been reported in several works (Riboux et al., 2010; Mercado et al., 2010; Roghair et al., 2011; Riboux et al., 2013).

The aforementioned works prevalently deal with pseudo-turbulence. A system closer to the one investigated here, is the very recent work of Prakash et al. (2016), which offers a compelling chance for a comparison against the numerical results presented here. This experiment, in fact, accounts for the contribution of bubble induced fluctuations as well as for the underlying turbulence. The set-up investigated in Prakash et al. (2016) consists of a homogeneous and isotropic turbulent flow of water in which air bubbles, in the range of 2 to 5 mm diameter, are inserted. It should be noted, however, that the corresponding single-phase flow Reynolds number based on the Taylor macroscale, Re_λ, investigated in Prakash et al. (2016) is equal to 170, which is higher than that of our numerical simulation at $y = H$ ($Re_\lambda = 34$) (Vreman and Kuerten, 2014). Furthermore, $Re_b = \mathcal{O}(10^3)$ has been simulated in Prakash et al. (2016). Despite the difference in Re and in the material properties, the core of the channel resembles characteristics of homogeneous turbulence, even more so when bubbles are present at high volume fraction (Fig. 4). Bearing in mind the important differences mentioned above, it is still interesting to qualitatively compare the results of our simulation with this experimental study. In addition, here we extend the investigation to a gas volume fraction of 10%, which is significantly higher then those analysed in Prakash et al. (2016).

3.4.1. Two- and one-dimensional spatial power spectra

The computation of the liquid kinetic energy spectrum requires particular attention. A straightforward approach would be to multiply the velocity field by the marker function $(1 - f)$, to sample only liquid region at a given time instance. However, the resulting spectrum would be convoluted with the spectrum of the step function, which is well known to introduce unphysical high frequencies. This phenomenon can be mitigated by replacing the sharp volume fraction field by a smooth equivalent $\tilde{f}$, which we here construct as the convolution integral of f with a Gaussian filter. The two-dimensional power spectrum of the stream-wise velocity, multiplied by $(1 - \tilde{f})$, is analysed in the mid vertical plane $y = H$. Fig. 13 shows the latter quantity for different volume fractions and for the single-phase flow as a function of the stream-wise wavenumber k_x. A Gaussian filter of width equal to 6 computational cells, which corresponds to about $D/4$, was used. Here, the wavenumbers are defined as the reciprocal of the wavelengths λ, rather than $2\pi/\lambda$.

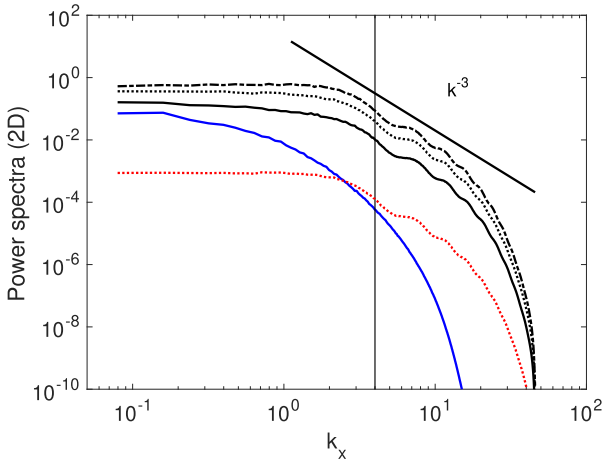

Fig. 13. Two-dimensional power spectra of $u_x(1-\tilde{f})$ at the plane $y=H$ as a function of the stream-wise wavenumber k_x. The solid black line is the profile for $\alpha=0.5\%$, the dotted line is the profile for $\alpha=2.5\%$, the dashed-dotted line is the profile for $\alpha=10\%$. The corresponding single-phase spectrum is indicated by the blue line. The power spectrum of $(1-\tilde{f})$ for $\alpha=2.5\%$ is indicated by the dotted red line for comparison. Slope k^{-3} is indicated as a reference. The vertical line indicates the wavenumber corresponding to $1/D$, with D the bubble diameter.. (For interpretation of the references to colour in this figure legend, the reader is referred to the web version of this article.)

For all examined volume fractions the spectra consist of an initially approximately constant profile followed by a decay well approximated by the -3 slope, which is subsequently replaced by a faster decay at higher wavenumbers. This profile is largely influenced by the power spectrum of the marker function, as is evident from the red dotted line reporting the spectrum of $(1-\tilde{f})$ for $\alpha=2.5\%$, which is also included in the figure. A model for the -3 scaling obtained by using the employed windowing technique is given in Appendix B.

An alternative way, which entirely avoids the influence of the windowing on the spectrum of the velocity signal, is that of computing the spectra of one-dimensional liquid filaments along the periodic directions (Ma et al., 2017). In Fig. 14 (left panel) an example of sampling of liquid filaments is shown. The corresponding single-phase stream-wise velocity is also shown (right panel of Fig. 14) for qualitative comparison.

The presence of low velocity regions due to the rising motion of the bubbles with respect to the liquid, the formation of wakes and their flow structure are clearly recognisable. As the volume fraction increases, the number of uninterrupted liquid filaments along the stream-wise direction drastically decreases, given the increased likelihood of finding a gas region along this path. Furthermore, the wakes are mainly aligned along the x-direction with the bubble paths and hence stream-wise liquid filaments may not contain information on the flow structures of the wakes. It is then of interest to also consider span-wise liquid filaments, which are more likely to account for the bubble wakes since the latter are crossed mainly orthogonally. The one-dimensional velocity signal of the filaments represented in Fig. 14 is shown in Fig. 15 and compared with the corresponding single-phase flow.

The presence of the wakes is clearly recognisable in the low velocity regions around $z\approx 2.3$ and 3.4. This feature is expected to influence the velocity power spectra. The latter, indicated as E_{xx}, are reported in Fig. 16. In order to have a relevant number of samples, the velocity signals have been collected in a core region equal to $0.85H<y<1.15H$ and $0.5H<y<1.5H$ for $\alpha=2.5\%$ and $\alpha=10\%$, re-

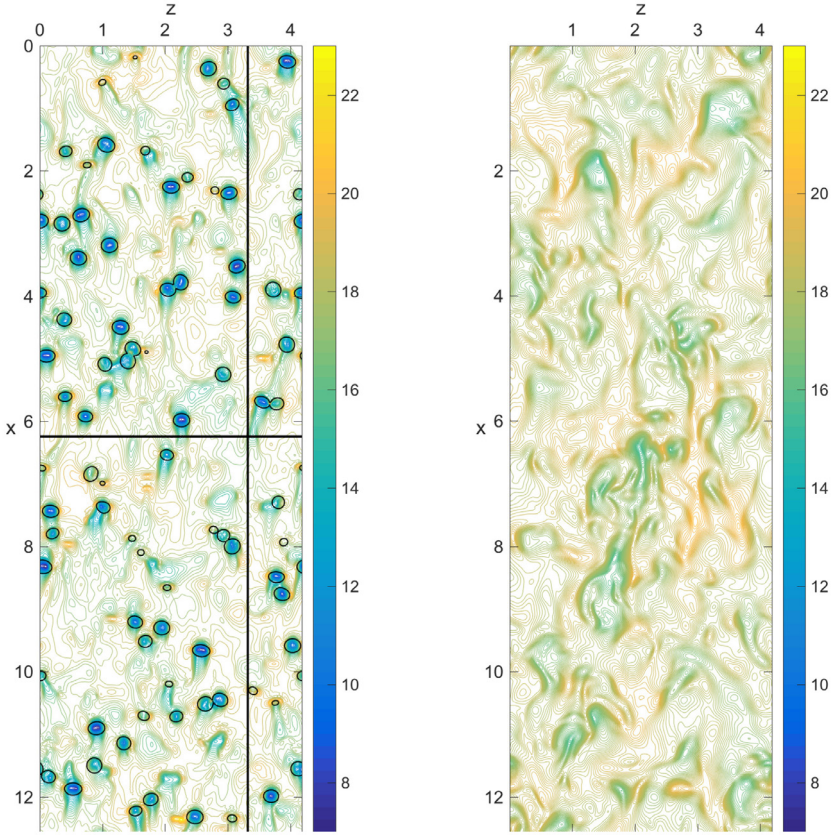

Fig. 14. Contours of the stream-wise velocity at $y=H$ for $\alpha=2.5\%$ (left panel) and for the single-phase flow (right panel). The contour $f=0.5$ is also shown to locate the bubble positions. An example of sampled stream-wise and span-wise liquid filaments is indicated by the black lines.

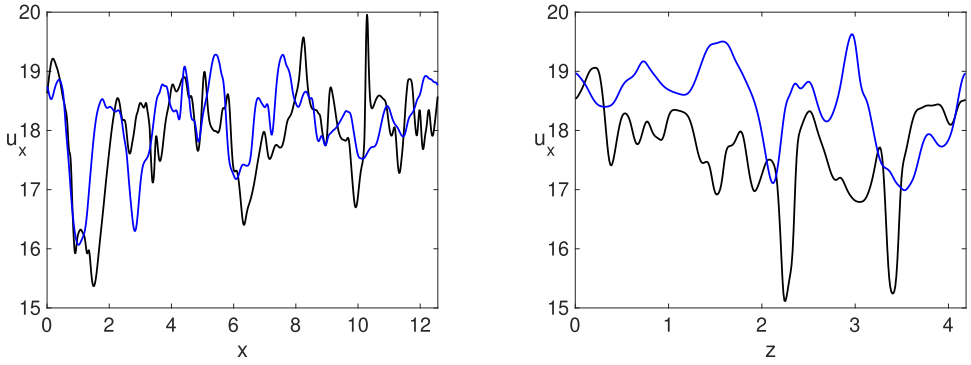

Fig. 15. Stream-wise velocity signal along the stream-wise (left panel) and the span-wise (right panel) direction of the filaments reported in Fig. 14 for $\alpha = 2.5\%$ (black line) and for the single-phase flow (blue line). (For interpretation of the references to colour in this figure legend, the reader is referred to the web version of this article.)

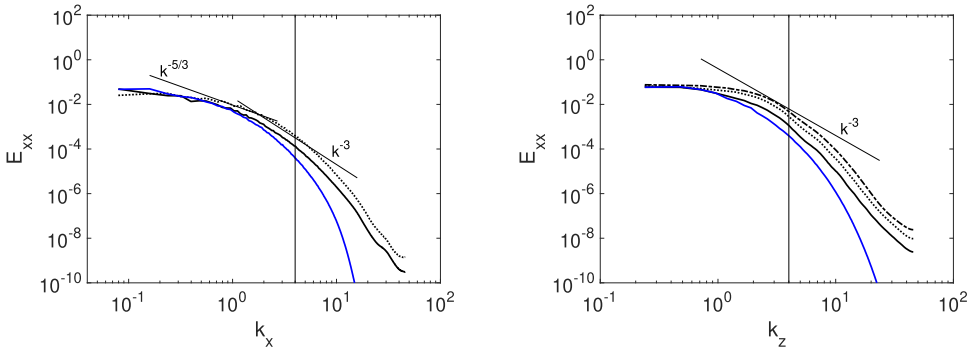

Fig. 16. E_{xx} spectra as a function of the stream-wise wavenumber k_x and span-wise wavenumber k_z. The solid black lines are the profile for $\alpha = 0.5\%$, the dotted lines are the profile for $\alpha = 2.5\%$, the dashed-dotted line is the profile for $\alpha = 10\%$. The corresponding single-phase spectra are reported by the blue lines. Slopes k^{-3} and $k^{-5/3}$ are indicated as a reference. The vertical line indicates the wavenumber corresponding to $1/D$, with D the bubble diameter. (For interpretation of the references to colour in this figure legend, the reader is referred to the web version of this article.)

spectively. For the most dilute case only the mid-plane velocity signals were computed. From the results presented in Section 3.1 we deduce that turbulence is approximately homogenous in those regions, which guarantees statistical equivalence of the considered velocity signals. In all cases, the spectra have been averaged over a number of segments > 50000. No liquid filament was obtained for $\alpha = 10\%$ along the stream-wise direction, hence only $E_{xx}(k_z)$ is available for the most dense case.

At sufficiently high Reynolds numbers the span-wise spectra of u follow Kolmogorov's $-5/3$ law in the inertial range, as shown in Bernardini et al. (2014) at $y/H = 0.3$ for $Re_\tau = 4000$. In the same work, the stream-wise spectra are found to closely follow a less steep slope according to a fit based on Re_λ. In our study, both the stream-wise and the span-wise spectra of the single-phase flow do not show a marked power law, but rather a continuously varying slope, which is attributed to low-Reynolds-number effects given that Re_τ is an order of magnitude lower than that analysed in Bernardini et al. (2014). The profile of $E_{xx}(k_x)$ for $\alpha = 0.5\%$ closely adheres to the corresponding single-phase spectrum until $k_x \approx 1.6$. At higher volume fraction ($\alpha = 2.5\%$), the stream-wise spectra show the $-5/3$ slope at wavenumbers $0.4 < k_x < 1.6$. This is consistent with the fact that the presence of bubbles enhances the turbulence intensity towards the core of the channel, as shown in Fig. 4. The $-5/3$ law of single-phase flow then transitions into a close to -3 slope in the narrow range from $k \approx 1.6$ up to $k \approx 4$. The latter k value corresponds to the wavenumber $k_D = 1/D$. This appears to be a cut-off point in our simulation from which the energy associated with smaller structures more rapidly decays toward the dissipative range. It should be pointed out, that the aforementioned scaling exists only for a very narrow wavenumber band and a marked scaling law could not be established.

As argued above, the span-wise spectra $E_{xx}(k_z)$ are expected to include a more significant portion of the bubble wakes compared to the stream-wise spectra. This is deducible from the right panel of Fig. 16 where a more significant deviation of $E_{xx}(k_z)$ from the single-phase span-wise spectrum is found also for the very dilute case. As α increases an initial and approximately constant spectrum is formed followed by a decay faster than k^{-3}.

The presented spectra agree, at best, only qualitatively with the experimental results of Prakash et al. (2016). Several differences arise. First, in the simulations we observe a gradual transition of the spectra from single-phase flow to the alterations in the most dense bubbly flow. This is consistent with the physical observation that, at low gas volume fractions, the turbulent kinetic energy content due to the liquid component is largely dominant over the bubbly energy content. In contrast, Prakash et al. (2016) reported a sudden change of the spectra regardless of the void fraction. Secondly, the -3 slope of the spectra found in Prakash et al. (2016), even though only approximately, extends for more than a decade, while here we observe a sharper decay towards zero energy content. This discrepancy could be explained by the higher Re considered in Prakash et al. (2016) with a corresponding shift of the Kolmogorov length scale towards higher k. Moreover, a transition frequency associated with the relative bubble velocity and the bubble diameter was proposed in Prakash et al. (2016) to explain the change of slope from $-5/3$ to -3. The findings presented here suggest that this transition occurs at wavelengths higher than D, even though only of approximately a factor 2.5 and hence of the same order of magnitude of that predicted by Prakash et al. (2016). It should also be noted that in Prakash et al. (2016) bubbles are polidispersed, which may have an influence on the cut-off wavenumber.

4. Conclusions

In this paper we have studied a fully developed turbulent channel flow at bulk Re equal to 6300, loaded with deformable spherical/ellipsoidal bubbles for three gas volume fractions: $\alpha = 0.5\%$, $\alpha = 2.5\%$ and $\alpha = 10\%$. In particular, a downflow channel, that is when the mean stream-wise velocity is aligned with gravity, was investigated. The latter configuration is characterised by a homogeneous region which extends wider in the core of the channel as the gas volume fraction increases. This allowed for a comparison with available studies on swarms of buoyant bubbles in a periodic cell at finite Re, referred to as pseudo-turbulence, both numerically (Bunner and Tryggvason, 2002a; 2002b) and experimentally (Mercado et al., 2010). By means of direct numerical simulation we accounted for all relevant physical mechanisms, including inertia, viscous effects and bubble deformability. With respect to previous studies on turbulent bubbly channel flow (Lu and Tryggvason, 2006; 2013), here we have considered a larger computational domain and included an order of magnitude more bubbles in the simulation making the statistical analysis more reliable. Furthermore, following the approach used by Bunner and Tryggvason (2002a,b) a detailed investigation of the bubble microstructure in terms of preferential bubble clustering and orientation has been carried out in the presence of underlying developed turbulence. The main findings are summarised in the following.

The liquid flow statistics, analysed in Section 3.1, show a moderate increase of the velocity fluctuations in the core of the channel especially pronounced for the rms of span-wise and wall-normal velocity fluctuations. A clear homogeneous region is observed in the core of the channel, which extends wider as the volume fraction increases. For the highest volume fraction ($\alpha = 10\%$) a strong turbulence attenuation close to the wall is found.

The radial pair distribution function showed the formation of clusters at close separation distances with a peak at $r/R = 2.2$, independently of the gas volume fraction. This suggests a close range attractive tendency among the bubbles that increases the short range coherency in the flow. On the contrary, in the profile reported by Bunner and Tryggvason (2002a) at $\alpha = 2\%$ the maximum was found to be absent at close distances with a corresponding low probability of collision. The different behaviour at low volume fractions has been attributed to the additional effect of the lift force, which drives the bubbles towards the core enhancing the clustering.

An inspection of the angular pair distribution function showed preferential horizontal alignment, more strongly at separation distances $r/R < 3$. While this is also observed in pseudo-turbulent studies (Bunner and Tryggvason, 2002a), significant differences are present for $\alpha = 2.5\%$. At $r/R = 4$, $G(\theta)$ is essentially uniform and close to 1, while in Bunner and Tryggvason (2002a) a strong horizontal alignment is still present. Moreover, as r increases, a general tendency for vertical alignment was found. This behaviour is more pronounced for the most dilute case investigated ($\alpha = 0.5\%$), qualitatively matching the experimental studies of Mercado et al. (2010). The larger number of bubbles and increased domain size may be important differences with earlier studies in this respect.

Attraction and repulsion between bubbles have been studied by analysing the probability of the relative radial velocity of a bubble pair being positive (Bunner and Tryggvason, 2002a). For $\alpha = 0.5\%$ a tendency to repulsion was observed for vertically aligned bubbles. This result is consistent with the theory and numerical findings of Yuan and Prosperetti (1994) for the motion of two vertically aligned bubbles. At the investigated Re_b (varying with α from 160 to 90), according to Yuan and Prosperetti (1994) an equilibrium distance can be found at values of r/R from approximately 4 to 5, below which the repulsive inertial effects are dominant. As the gas volume fraction increases, our results deviate from the theory of Yuan and Prosperetti (1994), with no significant dominant tendency to attraction or repulsion for $r/R > 4$. This highlights the influence of bubble interactions and of the underlying turbulence. From the same analysis on the meridian relative velocity of bubble pairs, we observed a general tendency for bubbles to rotate around each other and align horizontally, similar to what was reported in Bunner and Tryggvason (2002a).

The probability density functions of the bubble velocity fluctuations were found to be well approximated by the Gaussian distribution. This is in contrast with the pdf of pseudo-turbulence, which was shown to present significant differences from the normal distribution (Bunner and Tryggvason, 2002b; Mercado et al., 2010). We attribute the differences reported here to the interaction between the bubble motion and the base turbulence supplied by the channel flow.

In Section 3.4.1 the kinetic energy spectra of the liquid phase were investigated. First, we showed how a -3 slope of the power spectra can be an artificial effect of the windowing technique used to sample the liquid velocity. This issue was circumvented by collecting only one-dimensional spatial liquid segments providing a clear interpretation of the resulting spectra. Both stream-wise and span-wise power spectra were computed. The latter account for the presence of bubble wakes best. Our findings only resemble the experimental results on homogeneous and isotropic turbulence of Prakash et al. (2016), where a $-5/3$ law is gradually replaced by a -3 scaling. A marked scaling law was, in fact, not found in the analysed turbulent channel flow. Whether the differences observed here for bubbly turbulence with respect to previous studies on homogenous turbulence are due to the presence of the walls or due to lower Re remains an open question which will be the subject of future investigations.

Declaration of Competing Interest

The authors declare that they have no known competing financial interests or personal relationships that could have appeared to influence the work reported in this paper.

CRediT authorship contribution statement

P. Cifani: Conceptualization, Software, Formal analysis, Writing - original draft. **J.G.M. Kuerten:** Writing - review & editing. **B.J. Geurts:** Writing - review & editing.

Acknowledgements

This work was carried out on the Dutch national e-infrastructure with the support of SURF Cooperative. The Netherlands Organization for Scientific Research (NWO) is gratefully acknowledged for granting access to national supercomputer facilities.

Appendix A

In this appendix we provide an estimate of the statistical convergence of $g(r)$, $g(\theta)$ and the pdf's of the bubble velocity fluctuations, analysed in Sections 3.2 and 3.3, respectively. The following relative error measure is used:

$$E_r = \frac{1}{J}\sum_j \left(\frac{|q_j^{n+1} - q_j^n|}{|q_j^n|} \right), \tag{A.1}$$

where n corresponds to the simulation time over which the quantity q has been computed and $j = 1, .., J$ is the index of the point in the domain definition of q. The total averaging time and sampling rate have been specified in Section 3. Fig. A.17 shows error

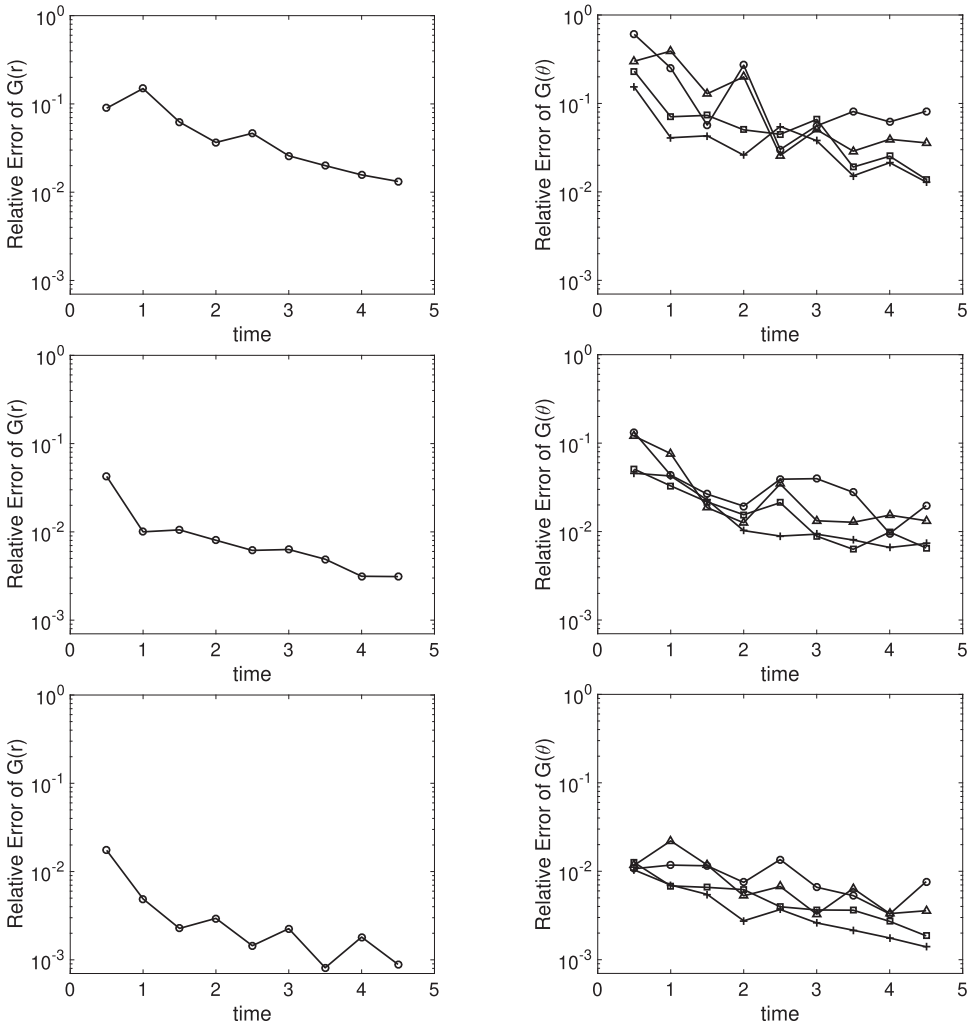

Fig. A.17. Error (A.1) of $G(r)$ (left column) and $G(\theta)$ (right column) as a function of the averaging time. The top figures refer to $\alpha = 0.5\%$, the center figures refer to $\alpha = 2.5\%$ and the bottom figures refer to $\alpha = 10\%$. For the angular pair distribution the following separation distances are shown: $r/R = 2.5$ (lines with circles); $r/R = 3$ (lines with triangles); $r/R = 4$ (lines with squares); $r/R = 5$ (lines with crosses).

E_r of the radial and angular pair distribution function for $\alpha = 0.5\%$, $\alpha = 2.5\%$ and $\alpha = 10\%$.

All the profiles show a relative error $\lesssim 1\%$ approaching zero faster as α increases, which indicates well converged statistical quantities.

Error (A.1) of the pdf's of the bubble velocity fluctuations is shown in Fig. A.18. The maximum relative error at the final averaging time is shown by the pdf of u_x' at $\alpha = 0.5\%$, being equal to 1.4%. All the other pdf's present a relative error $\leq 1\%$.

Appendix B

In this appendix we wish to illustrate the effect on the power spectrum of the windowing technique. To this end, a smooth window is built whose smoothing length is controlled by the convolution of the rectangular window with a Gaussian filter. In particular, an approach analogous to that employed in Risso (2011) is followed. Consider a one dimensional signal composed of a sequence of N rectangular windows:

$$h(x) = \sum_{n=1}^{N} H[(x - \bar{x}_n) + \delta_n] - H[(x - \bar{x}_n) - \delta_n], \tag{B.1}$$

where H is the Heaviside function, while $\bar{x}_n$ and δ_n are the position and the width of the $n-$th step, respectively. Function (B.1) can be interpreted as a typical one-dimensional marker function as well as the indicator function of a time signal extracted from an experimental probe (Lance and Bataille, 1983; Mercado et al., 2010). The Fourier transform of the convolution integral of $h(x)$ with the Gaussian filter $g(x) = \sqrt{\frac{a}{\pi}} e^{-ax^2}$ reads:

$$F(h * g) = \sum_{n=1}^{N} \frac{\sin(2\pi k \delta_n)}{\pi k} e^{-2\pi i k \bar{x}_n} e^{-\pi^2 k^2 / a}, \tag{B.2}$$

with a a constant and k the wavenumber, here defined as the reciprocal of the wavelength. Multiplication of (B.2) by its complex conjugate yields the power spectrum

$$s(k) = \frac{e^{-\frac{2\pi^2 k^2}{a}}}{\pi^2 k^2} \left[\sum_{n=1}^{N} \sin(2\pi k \delta_n)^2 + \sum_{n=1}^{N} \sum_{\substack{m=1,N \\ m \neq n}} \sin(2\pi k \delta_n) \sin(2\pi k \delta_m) \cos(2\pi k (\bar{x}_n - \bar{x}_m)) \right]. \tag{B.3}$$

As in Risso (2011), the parameters δ_n, δ_m, $\bar{x}_n$ and $\bar{x}_m$ are assumed to be independent random variables whose variation is independent of n. The ensemble average of $s(k)$ can be calculated as

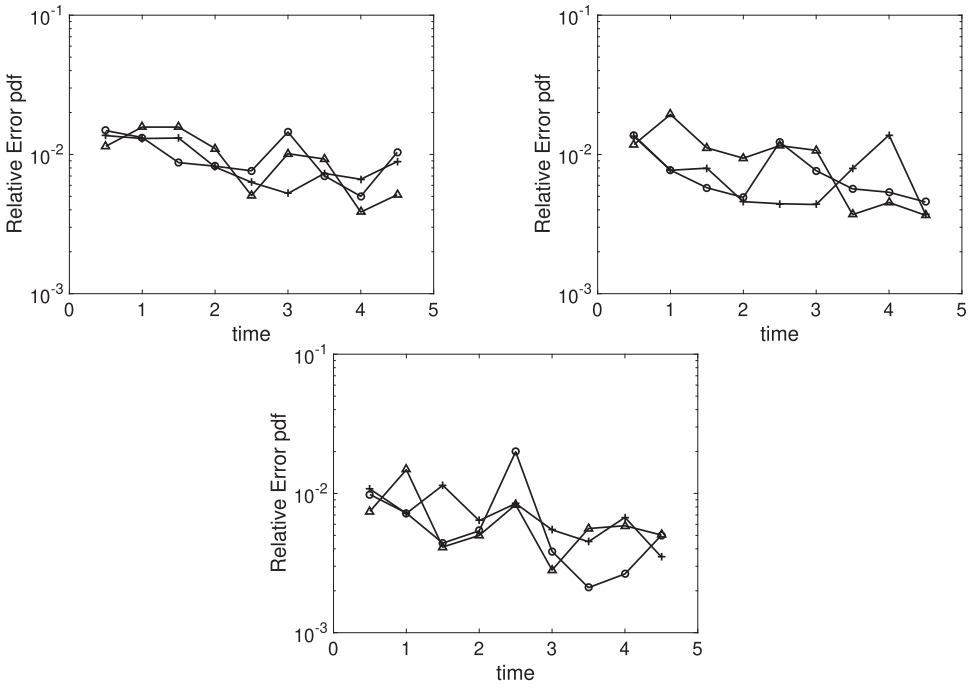

Fig. A.18. Error (A.1) of the pdf of stream-wise (lines with circles), the wall-normal (lines with crosses) and the span-wise (lines with triangles) bubble velocity fluctuations as a function of averaging time. The top-right figure are the results for $\alpha = 0.5\%$; the top-left figure are the results for $\alpha = 2.5\%$ and the bottom figure are the results for $\alpha = 10\%$.

follows:

$$\langle s(k)\rangle = \int_{\delta_{n,min}}^{\delta_{n,max}} \int_{\delta_{m,min}}^{\delta_{m,max}} \int_{\bar{x}_{n,min}}^{\bar{x}_{n,max}} \int_{\bar{x}_{m,min}}^{\bar{x}_{m,max}} \times s(k)\, p_\delta d(\delta_n)\, p_\delta d(\delta_m)\, p_{\bar{x}} d(\bar{x}_n)\, p_{\bar{x}} d(\bar{x}_m), \tag{B.4}$$

where p_δ and $p_{\bar{x}}$ are the probability density functions of the width and position of the Heaviside function, respectively. Assuming a uniform distribution of the latter parameters, Eq. B.4 reduces to

$$\langle s(k)\rangle = \int_{\delta_{n,min}}^{\delta_{n,max}} \int_{\delta_{m,min}}^{\delta_{m,max}} \int_{\bar{x}_{n,min}}^{\bar{x}_{n,max}} \int_{\bar{x}_{m,min}}^{\bar{x}_{m,max}} s(k) \frac{d(\delta_n)}{\Delta\delta} \frac{d(\delta_m)}{\Delta\delta} \frac{d(\bar{x}_n)}{\Delta\bar{x}} \frac{d(\bar{x}_m)}{\Delta\bar{x}}. \tag{B.5}$$

Analogously to the derivation of Risso (2011), the contribution to (B.5) of the second term of (B.3) can be made arbitrarily small by increasing the domain size $\Delta\bar{x}$ while keeping $N/\Delta\bar{x}$ constant. Hence, only the contribution from the first term of (B.3) is considered. The integral (B.5) reduces then to

$$\langle s(k)\rangle = \frac{N e^{-\frac{2\pi^2 k^2}{a}}}{8\pi^3 k^3 \Delta\delta} \times [\sin(4\pi k\delta_{min}) - \sin(4\pi k\delta_{max}) + 4\pi k(\delta_{max} - \delta_{min})]. \tag{B.6}$$

A Taylor expansion around $k = 0$ shows that $\langle s(k)\rangle$ is approximately constant at low wavenumbers. For $k \to \infty$ the spectra decays exponentially due to the Gaussian filter. There may exist, however, an intermediate range in which the exponential is still well approximated by unity and the term between square brackets in Eq. (B.6) is about constant. This leads to a local -3 scaling of the spectra. Assuming $\delta_{\min} \approx 0$, the term $-\sin(4\pi k\delta_{\max})$ approximately balances the increase due to the term $4\pi k\delta_{\max}$ from each crest to valley of the sinusoid. Thus, the starting wavenumber of the -3 scaling is approximately found at the first maximum of the sine function given by the condition $-\sin(4\pi k\delta_{\max}) = 1$, which yields

$$k_s = \frac{3}{8\delta_{max}}. \tag{B.7}$$

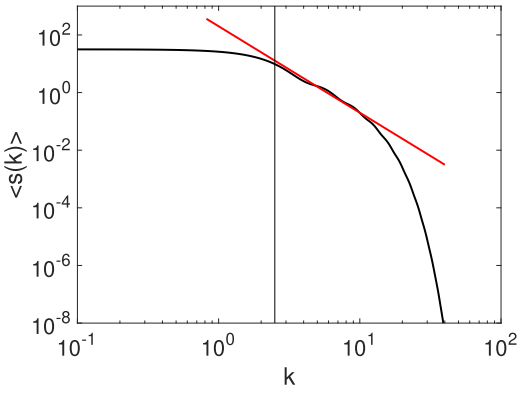

Fig. B.19. Power spectrum (B.6) as a function of the wavenumber. The -3 slope is indicated by the red line. The vertical line is the wavenumber k_s, as defined in (B.7). (For interpretation of the references to colour in this figure legend, the reader is referred to the web version of this article.)

This region may be further widened by the initial decay of the exponential which approximately compensates for the increase of the term between brackets of (B.6).

An example of $\langle s(k)\rangle$ is shown in Fig. B.19 for $\delta_{\max} = 0.15$, $\delta_{\min} = \delta_{\max}/20$, $N = 1000$ and $a = 2 \cdot 10^3$.

Is is worth noting that the -3 slope does not always appear. When the smoothing length of the filter increases, the damping of the Gaussian spectrum becomes dominant also at low wavenumbers hiding the -3 scaling. Vice-versa, as a increases the exponential decay is only relevant toward the far end of the spectrum. The -3 slope is, thus, quickly replaced by a -2 scaling, given by the ratio of the linear and the cubic term of Eq. (B.6) at high

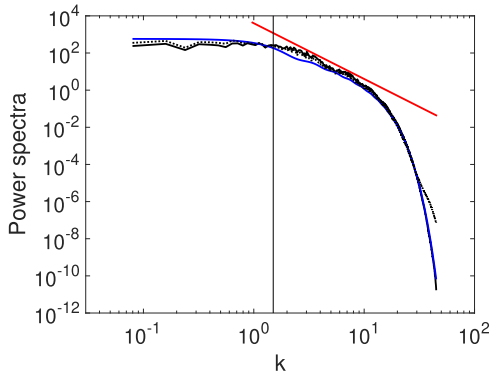

Fig. B.20. One-dimensional power spectrum of $(1-f_s)u_x$ (dashed-dotted line), of f_s (solid black line) and the analytical power spectrum (B.6) (blue line). The numerical spectra have been computed from segments in the mid-plane $y=H$ and scaled so to have the same underlying area. The red line indicates the -3 slope while the vertical line indicates the wavenumber k_s, as defined in (B.7). (For interpretation of the references to colour in this figure legend, the reader is referred to the web version of this article.)

enough values of k. In general, the intermediate range illustrated in Fig. B.19 will be present when the wavenumber at which the exponential decay starts to deviate from 1 is of the same order of magnitude as k_s. The latter requirement is mathematically expressed by $e^{-\frac{2\pi^2 k_s^2}{\bar{a}}} = 1-\epsilon$, with ϵ a small number, from which a corresponding value of a can be determined:

$$\bar{a} = -\frac{2\pi^2}{\ln(1-\epsilon)}\left(\frac{3}{8}\right)^2 \frac{1}{\delta_{max}^2}. \tag{B.8}$$

An additional requirement on the smoothing parameter a can be set by defining the spatial width of the Gaussian filter to be a fraction w of the maximum width of the rectangular window. In particular, at a distance $w\delta_{\max}$ the Gaussian is imposed to be qual to $10^{-p}g(x=0)$, with 10^{-p} a small number. The latter leads to

$$\bar{\bar{a}} = \frac{p\ln(10)}{(w\delta_{max})^2}. \tag{B.9}$$

Equating (B.8) to (B.9) yields

$$w = \sqrt{-\frac{p\ln(10)\ln(1-\epsilon)}{2\pi^2}\left(\frac{8}{3}\right)^2}. \tag{B.10}$$

As an example, setting $1-\epsilon = 0.963$ and $p=2$, a value of $w \approx 1/4$ is obtained. The same value of w was used in the results presented in Fig. 13.

An illustration of the effect of the windowing on the velocity field power spectrum is shown in Fig. B.20. The one-dimensional stream-wise power spectra of u_x, premultiplied by a smooth volume fraction field $(1-f_s)$, have been computed and averaged over the plane $y=H$ for $\alpha = 2.5\%$ (solid black line). The smoothing function f_s is obtained by the convolution of f with a Gaussian filter having a smoothing length equal to $D/5$. The spectra have been scaled so as to have the same energy content. Solution (B.6) well approximates the numerically computed spectra of f_s, as well as the starting wavenumber of the -3 slope. Furthermore, it is evident that the spectra of the liquid velocity is largely influenced by that of f_s.

Numerous sampling windows exist in literature, different from the one analysed here and often combined with averages of the periodigrams (Welch method (Welch, 1967)) for noise reduction. It is not the aim of this paper to generalise the above analysis to all such methods but rather to show how an artificial -3 scaling can be the result of signals selectively sampled with windows having a uniform width distribution. It would seem, thus, advisable to quantify this effect when employing such techniques.

References

Aland, S., Voigt, A., 2012. Benchmark computations of diffuse interface models for two-dimensional bubble dynamics. Int. J. Numer. Methods Fluids 69 (3), 747–761.

Bernardini, M., Pirozzoli, S., Orlandi, P., 2014. Velocity statistics in turbulent channel flow up to $re\_tau = 4000$. J. Fluid Mech. 742, 171–191.

Bunner, B., Tryggvason, G., 2002. Dynamics of homogeneous bubbly flows part 1. Rise velocity and microstructure of the bubbles. J. Fluid Mech. 466, 17–52.

Bunner, B., Tryggvason, G., 2002. Dynamics of homogeneous bubbly flows part 2. Velocity fluctuations. J. Fluid Mech. 466, 53–84.

Cheng, M., Hua, J., Lou, J., 2010. Simulation of bubble–bubble interaction using a lattice boltzmann method. Comput. Fluids 39 (2), 260–270.

Cifani, P., 2017. DNS of Turbulent Bubble-Laden Channel Flows Ph.D. thesis.

Cifani, P., 2019. Analysis of a constant-coefficient pressure equation method for fast computations of two-phase flows at high density ratios. J. Comput. Phys. 398, 108904.

Cifani, P., Kuerten, J.G.M., Geurts, B.J., 2018. Highly scalable DNS solver for turbulent bubble-laden channel flow. Comput. Fluids 172, 67–83.

Cifani, P., Michalek, W.R., Priems, G.J.M., Kuerten, J.G.M., van der Geld, C.W.M., Geurts, B.J., 2016. A comparison between the surface compression method and an interface reconstruction method for the VOF approach. Comput. Fluids 136, 421–435. doi:10.1016/j.compfluid.2016.06.026.

Coyajee, E., Boersma, B.J., 2009. Numerical simulation of drop impact on a liquid–liquid interface with a multiple marker front-capturing method. J. Comput. Phys. 228 (12), 4444–4467.

Dodd, M.S., Ferrante, A., 2014. A fast pressure-correction method for incompressible two-fluid flows. J. Comput. Phys. 273, 416–434.

Fakhari, A., Geier, M., Lee, T., 2016. A mass-conserving lattice boltzmann method with dynamic grid refinement for immiscible two-phase flows. J. Comput. Phys. 315, 434–457.

Francois, M.M., Cummins, S.J., Dendy, E.D., Kothe, D.B., Sicilian, J.M., Williams, M.W., 2006. A balanced-force algorithm for continuous and sharp interfacial surface tension models within a volume tracking framework. J. Comput. Phys. 213 (1), 141–173. doi:10.1016/j.jcp.2005.08.004.

Grace, J.R., 1973. Shapes and velocities of bubbles rising in infinite liquids. Trans. Inst. Chem. Eng. 51 (2), 116–120.

Gupta, A., Kumar, R., 2008. Lattice boltzmann simulation to study multiple bubble dynamics. Int. J. Heat. Mass. Transf. 51 (21–22), 5192–5203.

Hirt, C.W., Nichols, B.D., 1981. Volume of fluid (VOF) method for the dynamics of free boundaries. J. Comput. Phys. 39 (1), 201–225. doi:10.1016/0021-9991(81)90145-5.

Katz, J., Meneveau, C., 1996. Wake-induced relative motion of bubbles rising in line. Int. J. Multiphase Flow 22 (2), 239–258.

Kim, J., Moin, P., Moser, R., 1987. Turbulence statistics in fully developed channel flow at low reynolds number. J. Fluid Mech. 177, 133–166.

Kwakkel, M., Breugem, W.-P., Boersma, B.J., 2013. Extension of a clsvof method for droplet-laden flows with a coalescence/breakup model. J. Comput. Phys. 253, 166–188.

Lance, M., Bataille, J., 1983. Turbulence in the Liquid Phase of a Bubbly Air-water Flow. In: Advances in Two-Phase Flow and Heat Transfer. Springer, pp. 403–427.

Lau, Y.M., Deen, N.G., Kuipers, J.A.M., 2013. Development of an image measurement technique for size distribution in dense bubbly flows. Chem. Eng. Sci. 94, 20–29.

Liovic, P., Rudman, M., Liow, J.-L., Lakehal, D., Kothe, D., 2006. A 3d unsplit-advection volume tracking algorithm with planarity-preserving interface reconstruction. Comput. Fluids 35 (10), 1011–1032. doi:10.1016/j.compfluid.2005.09.003.

Lu, J., Biswas, S., Tryggvason, G., 2006. A DNS study of laminar bubbly flows in a vertical channel. Int. J. Multiphase Flow 32 (6), 643–660.

Lu, J., Tryggvason, G., 2006. Numerical study of turbulent bubbly downflows in a vertical channel. Phys. Fluids 18 (10), 103302.

Lu, J., Tryggvason, G., 2008. Effect of bubble deformability in turbulent bubbly upflow in a vertical channel. Phys. Fluids 20 (4), 040701.

Lu, J., Tryggvason, G., 2013. Dynamics of nearly spherical bubbles in a turbulent channel upflow. J. Fluid Mech. 732, 166–189.

Ma, T., Santarelli, C., Ziegenhein, T., Lucas, D., Fröhlich, J., 2017. Direct numerical simulation–based reynolds-averaged closure for bubble-induced turbulence. Phys. Rev. Fluids 2 (3), 034301.

Mercado, J.M., Gomez, D.C., Van Gils, D., Sun, C., Lohse, D., 2010. On bubble clustering and energy spectra in pseudo-turbulence. J. Fluid Mech. 650, 287–306.

Moser, R.D., Kim, J., Mansour, N.N., 1999. Direct numerical simulation of turbulent channel flow up to Re τ= 590. Phys. Fluids 11 (4), 943–945.

Popinet, S., 2009. An accurate adaptive solver for surface-tension-driven interfacial flows. J. Comput. Phys. 228 (16), 5838–5866. doi:10.1016/j.jcp.2009.04.042.

Popinet, S., 2018. Numerical models of surface tension. Annu. Rev. Fluid Mech. 50, 1–28.

Prakash, V.N., Mercado, J.M., van Wijngaarden, L., Mancilla, E., Tagawa, Y., Lohse, D., Sun, C., 2016. Energy spectra in turbulent bubbly flows. J. Fluid Mech. 791, 174–190.

Prosperetti, A., Tryggvason, G., 2007. Computational Methods for Multiphase Flow. Cambridge University Press.

Riboux, G., Legendre, D., Risso, F., 2013. A model of bubble-induced turbulence based on large-scale wake interactions. J. Fluid Mech. 719, 362–387.

Riboux, G., Risso, F., Legendre, D., 2010. Experimental characterization of the agitation generated by bubbles rising at high Reynolds number. J. Fluid Mech. 643, 509–539.

Rider, W.J., Kothe, D.B., 1998. Reconstructing volume tracking. J. Comput. Phys. 141 (2), 112–152. doi:10.1006/jcph.1998.5906.
Risso, F., 2011. Theoretical model for k^{-3} spectra in dispersed multiphase flows. Phys. Fluids 23 (1), 011701.
Roghair, I., Mercado, J.M., Annaland, M.V.S., Kuipers, H., Sun, C., Lohse, D., 2011. Energy spectra and bubble velocity distributions in pseudo-turbulence: numerical simulations vs. experiments. Int. J. Multiphase Flow 37 (9), 1093–1098.
Santarelli, C., Fröhlich, J., 2015. Direct numerical simulations of spherical bubbles in vertical turbulent channel flow. Int. J. Multiphase Flow 75, 174–193.
Santarelli, C., Fröhlich, J., 2016. Direct numerical simulations of spherical bubbles in vertical turbulent channel flow. Influence of bubble size and bidispersity. Int. J. Multiphase Flow 81, 27–45.
Scardovelli, R., Zaleski, S., 1999. Direct numerical simulation of free-surface and interfacial flow. Annu. Rev. Fluid Mech. 31 (1), 567–603. doi:10.1146/annurev.fluid.31.1.567.
Scardovelli, R., Zaleski, S., 2003. Interface reconstruction with least-square fit and split Eulerian–Lagrangian advection. Int. J. Numer. Methods Fluids 41 (3), 251–274. doi:10.1002/fld.431.
Tryggvason, G., Dabiri, S., Aboulhasanzadeh, B., Lu, J., 2013. Multiscale considerations in direct numerical simulations of multiphase flows a. Phys. Fluids 25 (3), 031302.
Uhlmann, M., 2008. Interface-resolved direct numerical simulation of vertical particulate channel flow in the turbulent regime. Phys. Fluids 20 (5), 053305.
Vreman, A.W., 2014. The projection method for the incompressible navier–stokes equations: the pressure near a no-slip wall. J. Comput. Phys. 263, 353–374.
Vreman, A.W., Kuerten, J.G.M., 2014. Comparison of direct numerical simulation databases of turbulent channel flow at Re $\tau =$ 180. Phys. Fluids 26 (1), 015102.
Wang, Y., Shu, C., Shao, J., Wu, J., Niu, X., 2015. A mass-conserved diffuse interface method and its application for incompressible multiphase flows with large density ratio. J. Comput. Phys. 290, 336–351.
Welch, P., 1967. The use of fast fourier transform for the estimation of power spectra: a method based on time averaging over short, modified periodograms. IEEE Trans. Audio Electroacoust. 15 (2), 70–73.
Wesseling, P., 2009. Principles of Computational Fluid Dynamics, 29. Springer Science & Business Media.
Yuan, H., Prosperetti, A., 1994. On the in-line motion of two spherical bubbles in a viscous fluid. J. Fluid Mech. 278, 325–349.